SANDIA REPORT
SAND2001-8186
Unlimited Release
Printed April 2000

LDRD Final Report: Exploiting LENS Technology Through Novel Materials

J. A. Brooks, C. V. Robino, M. L. Griffith, T. J. Headley, N. C. Y. Yang, S. H. Goods, D. F. Susan, and J. D. Puskar

Prepared by
Sandia National Laboratories
Albuquerque, New Mexico 87185 and Livermore, California 94550

Sandia is a multiprogram laboratory operated by Sandia Corporation, a Lockheed Martin Company, for the United States Department of Energy under Contract DE-AC04-94AL85000.

Approved for public release; further dissemination unlimited.

Sandia National Laboratories

Issued by Sandia National Laboratories, operated for the United States Department of Energy by Sandia Corporation.

NOTICE: This report was prepared as an account of work sponsored by an agency of the United States Government. Neither the United States Government, nor any agency thereof, nor any of their employees, nor any of their contractors, subcontractors, or their employees, make any warranty, express or implied, or assume any legal liability or responsibility for the accuracy, completeness, or usefulness of any information, apparatus, product, or process disclosed, or represent that its use would not infringe privately owned rights. Reference herein to any specific commercial product, process, or service by trade name, trademark, manufacturer, or otherwise, does not necessarily constitute or imply its endorsement, recommendation, or favoring by the United States Government, any agency thereof, or any of their contractors or subcontractors. The views and opinions expressed herein do not necessarily state or reflect those of the United States Government, any agency thereof, or any of their contractors.

Printed in the United States of America. This report has been reproduced directly from the best available copy.

Available to DOE and DOE contractors from
U.S. Department of Energy
Office of Scientific and Technical Information
P.O. Box 62
Oak Ridge, TN 37831

Telephone: (865)576-8401
Facsimile: (865)576-5728
E-Mail: reports@adonis.osti.gov
Online ordering: http://www.doe.gov/bridge

Available to the public from
U.S. Department of Commerce
National Technical Information Service
5285 Port Royal Rd
Springfield, VA 22161

Telephone: (800)553-6847
Facsimile: (703)605-6900
E-Mail: orders@ntis.fedworld.gov
Online order: http://www.ntis.gov/ordering.htm

SAND2001-8186
Unlimited Release
Printed April 2001

LDRD Final Report Report: Exploiting LENS Technology Through Novel Materials

J. A. Brooks, C. V. Robino, M. L. Griffith, T. J. Headley, N.C.Y. Yang, S. H. Goods, D. F. Susan, and J. D. Puskar

Abstract

Laser Engineered Net Shaping (LENS) is a direct fabrication process in which metal powders are deposited into a laser melted pool, with succeeding layers being deposited to build up complex engineering shapes. This process is a rapid, low cost, low footprint, direct fabrication technique that lends itself to the concept for advanced manufacturing. It is especially suited for rapid prototyping and small lot production. However, previous work has developed LENS as an advanced manufacturing tool, rather than exploiting its potentially unique attributes. These attributes include: real time control of microstructure, tailored material properties at different locations in the same part, the production of graded thermal expansion parts, etc. In this program, the important metallurgical parameters, solidification velocity and cooling rate, have been characterized and process models developed that are being used as input to microstructural models. Residual stresses were measured and process maps developed for controlling residual stresses and melt pool size that are critical for controlling part dimensions and quality. Tool steels and two stainless steels have been used as model systems to demonstrate the concept and feasibility of utilizing the high solidification velocities and cooling rates to design microstructures and properties to meet functionality. It has also been shown that starting powder characteristics can greatly affect build quality, especially intralayer porosity. Limited work on ceramic materials indicates that novel material can be fabricated using this technology. This work has added a new dimension in designing and fabricating engineering components with novel microstructures and properties using this rapid prototyping technology.

Contents

Abstract 3

Introduction 10

Section 1. Solidification Parameters: Velocity and Temperature Measurements 11

SAMPLE CONFIGURATIONS AND SOLIDIFICATION RATES 11
THERMOCOUPLE MEASUREMENTS 12
THERMAL IMAGING 13

Section 2. Residual stress measurements and process maps for stress 18

Predictions 18

BACKGROUND 18
HOLOGRAPHIC HOLE DRILLING RESIDUAL STRESS MEASUREMENTS 18
RESIDUAL STRESS PROCESS MAPS 20
SUMMARY 21
REFERENCES 22

Section 3. Feeding of Multiple Powders and Transition Structures 23

Section 4. Microstructural Evolution During LENS Fabrication of H13 Tool Steel 25

INTRODUCTION 25
APPROACH 25
SELECTION OF ALLOY SYSTEM 25
QUALITATIVE INTERPRETATION OF MICROSTRUCTURE EVOLUTION 28
MICROSTRUCTURE EVOLUTION IN THE SUPERCRITICAL REGION 29
MICROSTRUCTURE EVOLUTION IN THE SUBCRITICAL REGION 31
MICROSTRUCTURE EVOLUTION IN THE INTERCRITICAL REGION 35
SUMMARY 40
REFERENCES 40

Section 5. Aging Response of 17-4 PH Martensitic Stainless Steel LENS Deposits 42

EXPERIMENTAL 42
RESULTS AND DISCUSSION 43
SUMMARY 46
REFERENCES 46

Section 6. Microstructure Design of 304L Austenitic Stainless Steel 47

BACKGROUND 47
ALLOY DESIGN 47
EXPERIMENTAL RESULTS 49
TENSILE PROPERTIES 57
SUMMARY 58
REFERENCES 59

Section 7. Ceramic-to-Metal Transitions 61

INTRODUCTION 61
DIRECT METAL-TO-CERAMIC DEPOSITION 62
GRADED TRANSITIONS 62
METAL MATRIX COMPOSITES 63
SUMMARY 64

Section 8. Porosity in LENS Powders and Deposits **65**

PORE MORPHOLOGY AND DEPOSIT MICROSTRUCTURE 65
POROSITY CONTENT 67
MEASURED SIZE DISTRIBUTIONS 67
EFFECT OF REMELTING ON VOID REDUCTION 68
SUMMARY 69
REFERENCES 69

Section 9. Publications Funded, or Partially Funded, Under LDRD Program **70**

Report Summary **72**

Acknowledgements **72**

List of Figures

Figure 1.1. Schematics of shell (left) and block (right) builds. 11
Figure 1.2. Experimental set up for temperature measurements showing thermocouples that have been inserted into a shell build during different stages of processing. 12
Figure 1.3. Measured thermal cycles of H-13 shell build. 13
Figure 1.4 (a) fabrication of LENS wall build, (b) schematic of the ultra high speed digital imaging techniques. 14
Figure 1.5. High speed digital images taken from (a) top of laser melted pool (b) side view. 15
Figure 1.6. Data taken from 304L wall builds (a) temperature in the trailing direction of the melt pool for different laser powers (b) cooling rates near the solid liquid interface. 15
Figure 1.7. Melt pool lengths of wall builds of 304L stainless steel calculated by normalization scheme and compared with experimental measurements 16
Figure 2.1. Residual stress distribution along Z direction for three 316 stainless steel samples processed at different volumetric exposures (kJ/cm^3) 19
Figure 2.2. Relationship between maximum final stresses and process temperature gradient of 304 stainless steel for five different base temperatures. 21
Figure 3.1. Results obtained from graded transition from Ti-6Al-4V and the Ni-based superalloy IN 718. Phases were identified by EDS and Kukuchi pattern orientation imaging 23
Figure 4.1. Photograph of experimental setup for thermocouple measurement of LENS thermal cycles in shell build. 27
Figure 4.2. Measured thermal history for one location in H13 shell built at 5.9 mm/sec and 300 watts laser power 27
Figure 4.3. Optical micrograph of top edge of H13 shell build in relation to thermal cycles and H13 phase diagram. The height of one build pass is also shown on the micrograph and is approximately 0.25 mm. 28
Figure 4.4. TEM image of H13 LENS deposit showing bimodal distribution of carbides. A and B denote typical regions of V and Cr rich carbides, respectively 30
Figure 4.5. Microstructure of last pass of H13 shell build. 30
Figure 4.6 (a) Isothermal aging data for single line LENS deposits. (b) Correlation of data in (a) using Equations 7 and 8. 34
Figure 4.7. Gleeble dilatometry results for H13 steel heated at 100°C/sec 36
Figure 4.8. Diagram showing relationships between hardness and various heating regions. 36
Figure 4.9. (a) Comparison of measured and predicted hardness distributions in LENS H13 wall build. (b) Plot of calculated hardness as a function of peak temperature within the intercritical temperature range. 38
Figure 4.10. Tensile results showing 0.2% YS, UTS, and strain to failure of shell builds for nine process conditions: 200, 250 and 300 watts and 14, 18 and 22 ipm. 40
Figure 5.1. Hardness of 17-4 LENS block builds as deposited and after direct aging heat treatments for 4 hr. 43

Figure 5.2. Hardness of 17-4 LENS block builds as deposited, after solution heat treatment, and after aging for 4 hr. 44
Figure 5.3. SEM micrographs of fracture surface of an as-deposited tensile sample from a LENS shell build made at 20 ipm. (a) Low magnification showing porosity. (b) high magnification showing ductile microvoid coalescence. .. 45
Figure 6.1 Schematic of Fe- Ni-Cr pseudobinary showing approximately locations of the three alloys in Table 6.1 48
Figure 6.2. Microstructures of pulsed YAG laser welds in LENS builds: (a) in powder A showing primary austenite solidified microstructure (b) in powder B showing primary ferrite solidified fine grained austenite microstructure. 49
Figure 6.3 Two-phase structure of ferrite and austenite of primary ferrite solidified Block build made form powder of alloy A. Ferrite is in cores of dendrites. 50
Figure 6.4. Cross sections of build of powder A with a several percent Ni powder addition (a) upper portion of shell build showing a two phase primary ferrite structure at the outer surface and single phase primary austenite center region (b) higher magnification of (a), (c) single phase primary austenite solidified block build showing evidence of different layer and passes. 51
Figure 6.5 (a) STEM Image of primary austenite solidification structure in shell build of powder A alloyed with several % pure Ni showing region of analysis. Results for (b) Ni and (c) Cr 52
Figure 6.6. Microstructure typical of the shell builds with powder B. 53
Figure 6.7 Microstructures of block builds of alloy B (a) low magnification showing fine duplex grain structure and ferrite in HAZ of upper layer at top of micrograph (b) higher magnification showing microstructure typical of the majority of the build, (c) upper region of last deposited layer of build showing F/A solidification structure, arrow notes retained ferrite of dendrite cores.(d) retained solidification structure modified by multiple thermal cycles, similar to that in upper right of (a). 54
Figure 6. 8. Microstructures of block build of powder C: (a) fine grain, nearly single phase austenite structure (b) common HAZ region of two overlapping passes showing retained ferrite (c) top or last layer of build showing solidification structure associated with an individual power particle, and to the left small region of ferrite at interpass boundary 55
Figure 6.9. TEM microstructure of block builds of powder B showing (a) thin films of ferrite along regions of the austenite grain boundaries, (b) islands of intragranular ferrite 56
Figure 6.10. STEM analysis of block build of powder B (a) STEM image showing region of analysis, (b) Cr (c) Ni results. 57
Figure 7.3. Optical micrographs of titanium LENS deposit containing dispersed Al_2O_3 particles. Note the particles retain their angular features and are not cracked. 64
Figure 8.1. Photomicrographs of as-polished (a) 17-4PH and (b) 304L-4 LENS powders. 65

Figure 8.2. (a) Photomicrograph of interlayer lack of fusion in 304L-3, block LENS build. (b) Cross-section of 17-4PH, shell build showing spherical porosity. (c) Low magnification photomicrograph of spherical porosity in 304L-2, block build. Note smaller size and amount of pores in 304L compared to 17-4PH.(d) Higher magnification view of spherical porosity (differential interference contrast). 66
Figure 8.3. Porosity measurements in powders and LENS builds: (a) shell builds, (b) block builds. Laser travel speed was 100 cm/min for all deposits. 67
Figure 8.4. (a) Summary histograms of voids within starting LENS powders. (b) Ratio of average void volume to average particle volume for LENS powders. 68
Figure 8.5. Photomicrograph of top layers of 17-4PH LENS deposit (etched condition). On right side of image, the top 1-2 LENS layers have been remelted. 69

List of Tables

Table 4.1 Composition of H13 Tool Steel Powder. 26
Table 5.1 Composition of 17-4 Powder. 42
Table 6.1 Heat compositions and Cr_{eq}/Ni_{eq} ratios 48
Table 6.2 Tensile Properties 58

Introduction

The concept of near net shape fabrication using additive processes like LENS is an intriguing concept that is now starting to experience early rapid prototyping and production applications. However, it was recognized that much of the early work had been dedicated to the development of CAD programs and the process engineering required to prove this a viable technique to be used for rapid prototyping. Very little work had been done in understanding the metallurgical characteristics and the potential this process may have for producing unique components with novel microstructure and properties. The goal of this LDRD was to determine to what extent this capability may exist. Paramount to this task was the development of the understanding of the important solidification parameters, solidification velocities, cooling rates and thermal environments. It was also recognized that thermal stresses were important to both part performance as well as dimensional tolerances. Furthermore it was recognized that for some novel material development such as transitions from metals to ceramics management of thermal stresses would be critical. The ability to tailor unique microstructures and properties, and the ability to process for properties would be a very important attribute for the success of the LENS process. It was recognized that this would require the integration of the process attributes, solidification velocity and cooling rates, and alloy design that would exploit these attributes. This report summarizes, in individual sections, different aspects of the program. More complete details of the work funded under this program are contained in the publications listed in the last section of the report.

Section 1. Solidification Parameters: Velocity and Temperature Measurements

Sample Configurations and Solidification Rates

One of the first goals of the program was to develop a thorough understanding of the LENS process in terms of how it impacts solidification and microstructure development. Solidification velocity and cooling rates are the two main parameters which are required to develop and predict microstructures, but which had not been characterized in the LENS process. It was decided in the beginning of the program that two sample configurations would be used: shells and blocks shown schematically in figure 1.1. Single-width line deposits were used to build 6.35 cm square layered shells several cm high. The size of each individual layer was approximately 0.25 mm high and ~ 0.75 mm wide. Solid blocks 7.6 cm long and 9.5 mm wide were built using parallel multipass layers with passes oriented at 90° between each layer. The height of each layer of the several-cm high deposit was approximately 0.25 mm, and the individual pass width within the layers was approximately 0.4 mm. It should be noted that the actual dimensions of the laser passes were dependent on the specific processing parameters with the size of the individual passes decreasing with increasing travel speed and decreasing laser power. In several cases other configurations were used which included a single line width wall build. It was found with stainless steel and H-13 tool steel powders that solid builds of both configurations could be made with travel speeds from ~ 4.2 to 33.9 mm/s (~10 to 80 ipm). Laser powers ranged from ~ 200 to 700 watts with the 1 kW continuous YAG laser. The higher powers were used for the higher speed builds. Although this range in travel speeds may be extended, it was sufficiently wide for tailoring build microstructures. When modeling solidification, knowledge of the solid-liquid interface and dendrite tip velocity is also required. However, these can be determined knowing travel speed, melt pool shape and dendrite orientation.

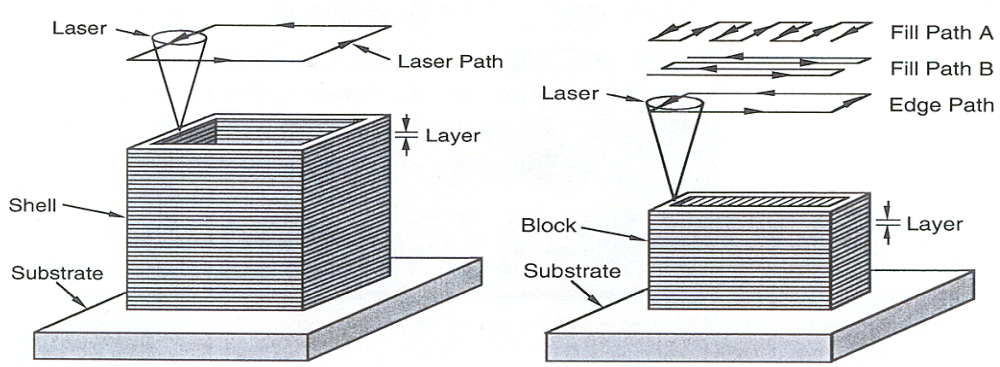

Figure 1.1. Schematics of shell (left) and block (right) builds.

Thermocouple Measurements

A relatively easy way to obtain the thermal history during LENS processing is by inserting thermocouples (TC) directly into the sample during fabrication. Fine diameter (250 micron) Type C thermocouple wire was used for measurements with care taken to insert the TC bead into the deposition zone for accurate temperature measurements. A photograph of the experimental set-up is shown in figure 1.2. Figure 1.3 shows typical temperature readings for twenty deposition layers from a representative thermocouple inserted during fabrication of an H13 tool steel shell build made at a travel speed of 7.6 mm/s. Each peak in temperature represents the thermocouple response as the laser passes over or near the thermocouple, from initial insertion through subsequent pass depositions. The thermal excursions dampen out when either the energy source moves away from the thermocouple during fabrication of a layer or subsequent layers are deposited. After the initial peak in temperature, approximately 1500 °C, the heat is quickly conducted away in about 15 seconds to a nominal value of 150 °C for the first layer. Each subsequent pass reheats the previous layers, such that after the fifth single pass layer is deposited, the thermocoupled layer still receives thermal excursions to 900 °C. After thirteen deposition layers, the peak temperature is 500 °C. The resolution of the time scale shown in the figure is not sufficient to determine the accurate cooling rate. However, the point to be made is that once a pass is deposited, the material experiences a number of high temperature thermal cycles that may control the final microstructure and residual stresses. At higher resolution, the maximum cooling rates after solidification were determined to be ~3500 °C/sec. These were the first temperature measurements on LENS fabricated parts that showed cooling rates should be sufficiently fast to allow the tailoring of unique microstructures. This cooling rate is of course dependent upon processing conditions. Similar measurements were made on block builds that also recorded the multiple thermal cycles. In block builds cooling rates even higher than those obtained with shells were obtained.

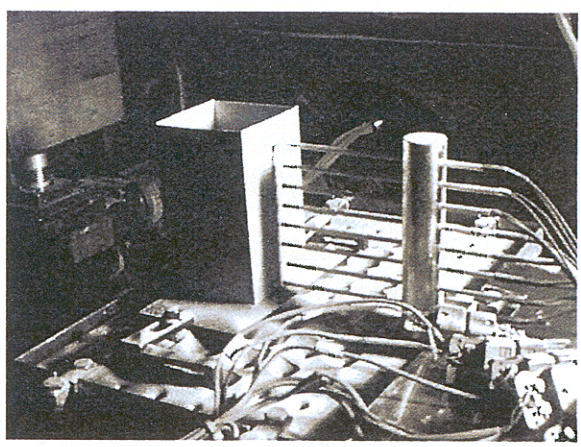

Figure 1.2. Experimental set up for temperature measurements showing thermocouples that have been inserted into a shell build during different stages of processing.

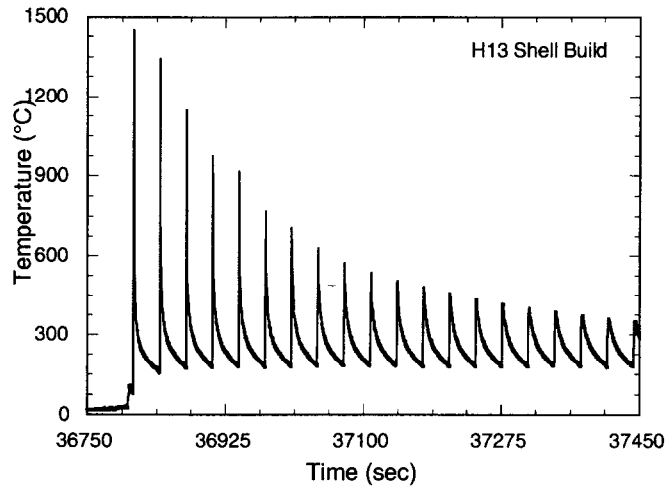

Figure 1.3. Measured thermal cycles of H-13 shell build.

Thermal Imaging

Although thermocouples can very accurately measure cooling rates, it was desirable to develop a better understanding of the thermal field in the region of the liquid pool. It is known that thermal gradients exist across the molten pool and into the bulk material created by the LENS process. However, the nature and extent of these gradients had not been previously characterized. It was desirable to use non-invasive thermal imaging to measure the temperature profile and gradients and to possibly use these thermal profiles in a feedback control scheme.

Collaborating with Prof. William Hofmeister of Vanderbilt University, localized thermal measurements were made on a single line wall build, using ultra high speed digital imaging techniques [1,2]. For the LENS studies, a digital 64x64 pixel CCD video camera was employed. This camera digitizes monochrome images to 12-bits and passes the frame data to a personal computer for storage and processing. A telephoto lens and broad band-pass filter centered at 650 nm were used in the image path. The camera, lens, and filter were calibrated for temperature measurement with a tungsten strip lamp radiance source obtained from the National Institute of Standards and Technology. A picture of the LENS process, figure 1.4a and schematic of the experimental setup is shown in figure 1.4b. The powder and laser focus do not move in the x-y plane so that the build could be tracked by adjusting the tilt of the camera. The camera angle was measured with a clinometer and was adjusted as the build progressed. Images were taken at up to 990 frames per second. At the end of each set of imaging experiments, a molten pool was formed with no translation of the work piece to observe the freezing plateau for *in situ* calibration.

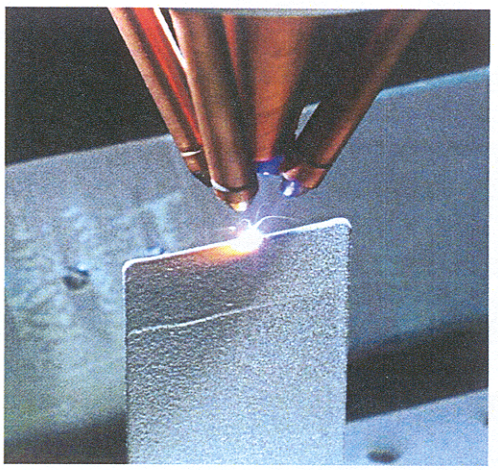

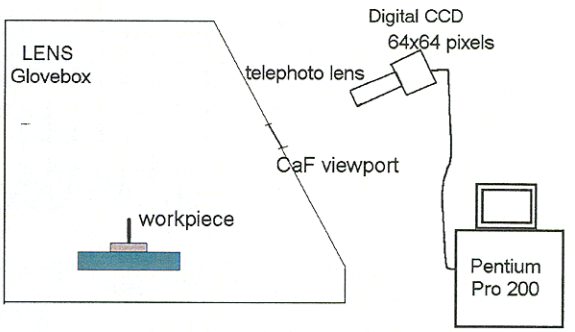

(a) (b)

Figure 1.4 (a) fabrication of LENS wall build, (b) schematic of the ultra high speed digital imaging techniques.

Figure 1.5a shows a typical view of the molten pool as seen from the top. The image has been converted to temperature according to the adjacent scale. In the figure, the bead motion is from top to bottom, as signified by the thermal tail. The solidification interface, or pool area, at 1650 K is outlined and is monitored in real time. Note the relatively high degree of superheat within the molten pool (greater than 250 K), that will effect the thermal gradients at the solid liquid interface and solidification microstructures. The temperatures in regions behind the laser pool can also be determined, figure 1.6a.

A typical side view image of a line build is shown in figure 1.5b. The image has been converted to temperature according to the adjacent scale. The angle of the image to the x-y plane is approximately 30° so that the top surface as well as the front face of the build is visible. Since the angle of the plane of the camera to the sample is known, the distances and temperatures can be corrected for the angle of view. Images of the kind shown in figure 1.5 were analyzed to determine the isotherms on the side-wall of the build. The gradients in the previous build layer below the laser are as high as 400K mm^{-1} and taper off to less than 200K mm^{-1} in the trail of the molten pool. Since the sample is moving in the x-direction, it is also possible to scale these gradients with the sample velocity to derive cooling rates for material deposited in the x-direction.

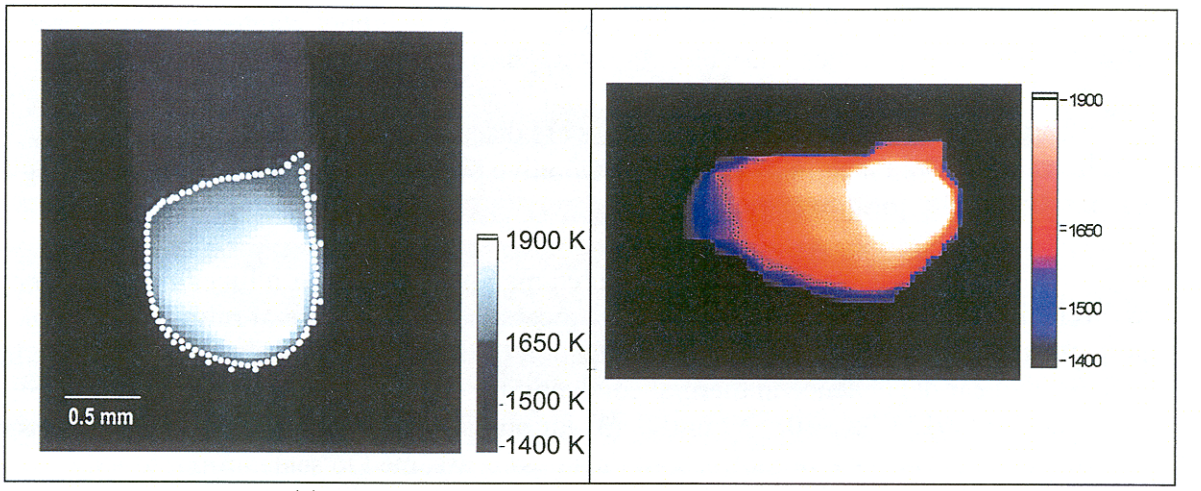

(a) (b)

Figure 1.5. High speed digital images taken from (a) top of laser melted pool (b) side view.

A complete series of wall builds was analyzed to determine the cooling rate at the solid-liquid interface. These determinations are shown in figure 1.6b. At the interface the cooling rates are substantially higher at the low power levels and remain fairly constant at the higher powers. Thus, the highest cooling rates are achieved at the lowest power, when the molten zone is small. As the laser power is increased, the cooling rate at the interface settles at 1000-1500 K/s. With information about temperatures in and around the molten pool, pool size, and thermal gradients, it may be possible to utilize in-situ control to improve the capabilities of parts fabricated by LENS.

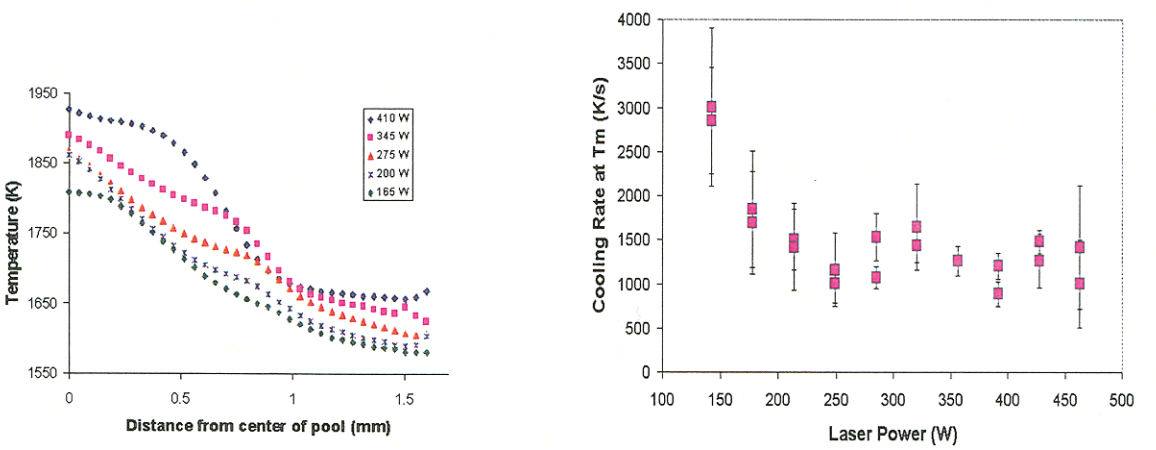

Figure 1.6. Data taken from 304L wall builds (a) temperature in the trailing direction of the melt pool for different laser powers (b) cooling rates near the solid liquid interface.

Analytical Solutions for Temperatures

Analytical solutions for a 2-D conductive heat transfer solution for a point heat source moving across a semi-infinite substrate developed by Rosenthal [3] has been used for many welding applications. These solutions are also applicable to shell and wall builds made with

the LENS process. As suggested by these solutions the melt pool length can be represented through three dimensionless variables: the normalized melt pool length, the normalized height of the substrate, and the normalized melt temperature. The normalization technique and assumptions made for the LENS process are discussed in detail in SAND reports by Dykhuizen and Dobranch [4,5] and in collaborative papers with Prof. J. Beuth of Carnegie Mellon University [6,7].

Figure 1.7 provides a comparison of measured melt pool lengths as a function of laser power and velocity to predictions provided by the process maps using several rules: (1) thermal properties at 1000K are used in the normalization (2) for changes involving a difference in preheat, a linear dependence in thermal conductivity with a preheat temperature is assumed as: $k = 24.3 + 0.013\ (T_{base}-30)$ W/mmK) (3) for predicting steady-state melt pool lengths due to a change in processing variables, wall thickness is assumed to scale proportionally with melt pool length, and (4) it is assumed that the melt pool length/wall thickness scaling is unaffected by velocity. The only inputs used to generate the predictions from the process map were a single experimentally measured wall thickness of $t = 1.3$ mm for ambient conditions of $V = 7.6$ mm/s and $\alpha Q = 105$ W where Q is laser power and α fraction of laser power absorbed by the wall) $\alpha = 0.35$ as suggested by Dorbranich and Dykenhuizen(4,5). Measurements were made using the real-time thermal imaging methods described above. The experimental results presented are for a single set of observations and reflect the variability seen in measured results at nominally identical conditions, which can easily be on the order of 5%. Because α is not known precisely, caution is suggested in directly comparing measured and predicted values. However, the predictions of the process map are clearly capturing the trends in the measured results, which was a goal of this work.

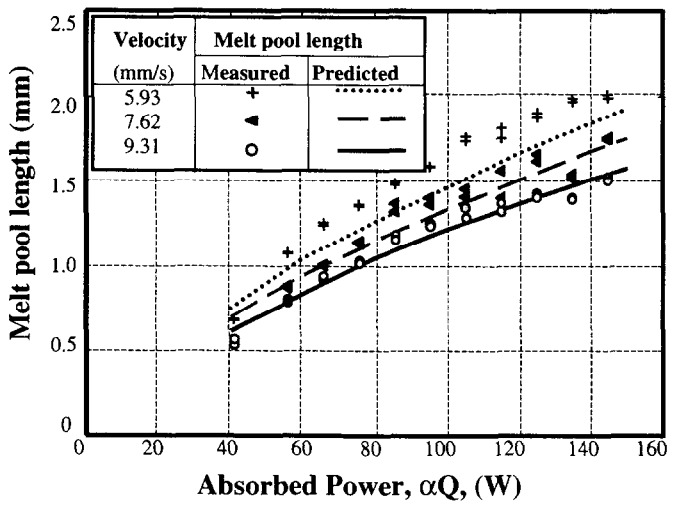

Figure 1.7. Melt pool lengths of wall builds of 304L stainless steel calculated by normalization scheme and compared with experimental measurements

Summary

The solidification velocities and cooling rates measured here show that the LENS process do not approach the regime of rapid solidification processing that is common in technologies such as melt spinning, laser welding, laser surface heat treating or laser glazing. With these technologies velocities can be on the order of m/s with cooling rates to as high as 10^{-5} to 10^{-6} K/s. The lower solidification velocities and cooling rates are of course due to the fact that LENS is an additive manufacturing process where a melt pool must be established with sufficient superheat to completely melt the incoming powder. Nevertheless, rates may still be sufficiently fast to obtain tailored microstructure in specially designed alloy systems. The thermal measuring techniques developed can be used to provide the critical metallurgical parameters required for microstructural predictions.

The experimental techniques also provide the necessary work to validate more complex thermal models in addition establishing their potential for use in feed back control schemes where temperature or temperature measurements are related to some critical attribute of the build. The analytical solution using normalization schemes, clearly demonstrate the value of this approach in relating process parameters to build attributes.

References

1. W. Hofmeister, M. Wert, J Smugeresky, J. Philliber, M. Griffith, and M. Ensz Investigation of Solidification in the Laser Engineered Net Shaping (LENS™) Process, *JOM*, Vol. 51, No.7, 1999
2. M. L. Griffith, M. E. Schlienger, L. D. Harwell, M. S. Oliver, M. D. Baldwin, M. T. Ensz, J. E. Smugeresky, M. Essien, J. Brooks, C. V. Robino, W. H. Hofmeister, M. J. Wert, D. V. Nelson, *Thermal Behavior in the LENS Process*, proceedings of the Solid Freeform Fabrication Symposium, August, 1998, Austin, TX, p. 89.
3. D. Rosenthal, "The Theory of Moving Sources of Heat and Its Application to Metal Treatments," *Transactions of ASME*, Vol. 68, 1946, pp. 849-866.
4. Dykhuizen, R.C. and Dobranich, D., "Cooling Rates in the LENS Process," Sandia National Laboratories Internal Report, 1998.
5. Dykhuizen, R.C. and Dobranich, D., "Analytical Thermal Models for the LENS Process," Sandia National Laboratories Internal Report, 1998.
6. A.Vasinonta, J. L. Beuth, M. L. Griffith, *A Process Map for Consistent Build Conditions in the Solid Freeform Fabrication of Thin-Walled Structures*, accepted to Journal of Manufacturing Science and Engineering, July 2000.
7. J. Beuth, A. Vasinonta, and M. Griffith, *Process Maps for Laser Deposition of Thin-Walled Structures*, proceedings of the Solid Freeform Fabrication Symposium, August, 1999, Austin, TX, p. 383-391.

Section 2. Residual stress measurements and process maps for stress Predictions

Background

Residual stress-induced tolerance loss is a concern in nearly all solid freeform fabrication (SFF) processes. This includes processes based on successive curing of polymers as well as those based on successive thermal deposition of polymers or metals such as LENS. In using these processes for rapid prototyping, some tolerance loss due to residual stresses is generally acceptable; however, many targeted applications for manufacturing techniques have strict dimensional limits. Residual stress-induced deformation is also becoming a greater concern with the fabrication of large parts, where larger part dimensions naturally lead to larger dimensional losses. The knowledge of residual stress magnitude and distribution is also of interest since they can play a significant role in structural performance. Thus it was clear that a better understanding of residual stresses in LENS fabrication was required, and this was a major milestone in the LDRD program.

Holographic Hole Drilling Residual Stress Measurements

In collaboration with Prof. Drue Nelson at Stanford University [1,2], a holographic-hole drilling technique [3] was used to determine the residual stress state in the LENS fabricated samples. In the holographic-hole drilling method, a region of a test object containing stress is illuminated with laser light. A hologram of the region is made by exposing a recording plate in a commercially available holocamera to the light of a reference beam and that of the object beam as reflected from the test object. The hologram is recorded electrostatically on an erasable, re-useable thermoplastic medium. Then a small square-bottomed hole is milled into the region of interest to a depth that can be varied, but which is generally a fraction of the hole diameter. The hole releases residual stresses locally, causing material surrounding the hole to deform in response to the stress relief. The resulting surface deformations, which are both in-plane and out-of-plane, alter the path length of the light reflected from the region, immediately creating a pattern of optical interference fringes on the hologram. The interference fringe pattern can then be analyzed to determine the residual stresses that existed prior to the introduction of the hole.

Figure 2.1 summarizes some of the residual stress results obtained on 316 stainless steel [1]. These measurements were taken on rectangular solid builds (X =Y = 0.5 inches, Z ~2 inches) made at several laser powers, and traverse velocities. Also shown is the corresponding volumetric exposure or heat input. In these samples, the residual stresses are high near the substrate, 50 ksi, but decreases rather sharply after ~15 mm build height. During initial fabrication the substrate efficiently conducts the laser-generated heat from the LENS sample, resulting in a large thermal gradients and higher residual stress state. As the substrate and the

LENS part are heated during fabrication, the thermal gradient is reduced, and the residual stresses diminish.

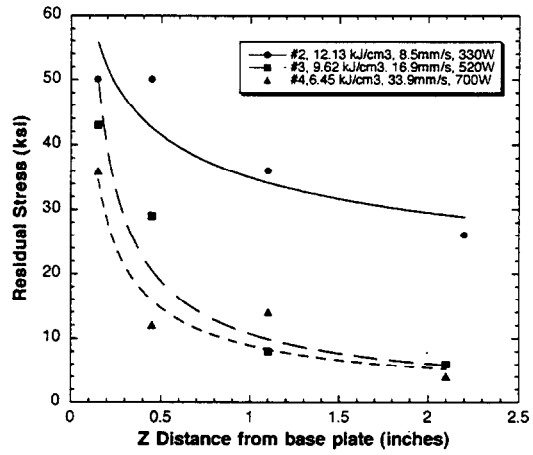

Figure 2.1. Residual stress distribution along Z direction for three 316 stainless steel samples processed at different volumetric exposures (kJ/cm^3).

It can be seen that the highest residual stresses correspond to the highest volumetric exposure (kJ/cm^3), and also in this case, to the highest heat input calculated as the ratio of laser power to traverse velocity (linear heat input). The measured maximum residual stresses near the substrate approach the ~60 ksi yield strength of 316 LENS deposits.

The residual stresses in the LENS deposits were also found to be highly dependent upon alloy type. For example, similar residual stress measurements were made on H13 tool steel [2] that has a yield strength three times that of the 316 stainless steel alloy. In this material measurements were made on both the shell and block configurations shown in Section 1, figure 1.1. In the shell builds the measured major principal stresses never exceeded ~35 ksi and in many cases were less than 15 ksi. Unlike those of the 316 samples, the magnitude of the stresses were uniform from the substrate to the top of the over 4 inch high build. With the block builds, maximum measured principal stresses never exceeded 30 ksi and in some regions measured stresses were actually compressive. In both build types the maximum measured residual stress were less than 20% of the measured yield strengths of 150 to 200 ksi.

The difference in the stresses of the two alloy types, 316 and H13, are directly related to the solidification and transformation behavior. At high temperatures, the 316 stainless steel is FCC austenite and retains that structure to room temperature. During cooling, the strains that occur due to thermal contraction are dependent upon thermal gradient. At elevated temperatures these strains are easily accommodated by plastic flow in the low strength material. As the material continues to cools, and flow stress increases until at room temperature the residual stresses are often on the order of the yield strength when processing is conducted under high thermal gradients. Of course, in addition to the magnitude of the

temperature and thermal gradients, metallurgical and geometrical factors play a complex role on the final magnitude and direction of principal stresses.

Alloy H-13, like alloy 316 is also FCC austenite at high temperature, and residual stresses are developed on cooling in the same fashion as that described for 316. However, when the temperature reaches ~300 to 250°C the material transforms to a BCT martensitic structure. This transformation results in a volumetric expansion of ~ 4.3%. This expansion relieves a large fraction of the tensile stresses and as indicated by the residual stress measurements, can even result in the stresses being compressive. However it must be recognized that development of the final residual stresses is very complicated is the result of numerous and complex thermal cycles.

Residual Stress Process Maps

In a manner similar to that used to develop process maps for temperature and thermal gradients in Section 1, process maps were also developed for residual stress in collaborative work with Prof. Beuth of Carnegie Mellon University. The same normalization approach used for temperature and thermal gradient was extended to residual stresses and has been published in the open literature [4,5].

Through the normalization scheme used, the actual temperature gradient is given by:

$$\left.\frac{\partial T}{\partial Z_0}\right|_{\bar{Z}_0=1.2} = \frac{\rho c V \alpha Q}{2\pi k^2 t} \left.\frac{\partial \bar{T}}{\partial \bar{Z}_0}\right|_{\bar{Z}_0=1.2}$$

(where Z_0 is direction down from the surface of the build, ρ = density, c = specific heat, V = travel speed, Q = laser power, α = fraction of laser power absorbed by the wall, Z_0 =1.2 normalized distance).

Thus, for a fixed normalized temperature gradient, $\left.\frac{fT}{f\bar{Z}_0}\right|_{\bar{Z}_0=1.2}$ is decreased by a decrease in V.

Figure 2.2 gives results for $\sigma_{max}/\sigma_{yield}$ of 304 stainless steel as a function of actual temperature gradient from thermomechanical simulations of the wall builds using five different base plate temperatures and the full range of laser power and velocity. The plot shows the dependence of residual stress on temperature gradient. Considering the results generated for a base plate temperature of 400 K, it is seen that different sets of process parameters produce approximately the same maximum stresses in the part if the representative temperature gradients are matched. Also, as expected, at a fixed base temperature, the residual stresses decrease with decreasing temperature gradient.

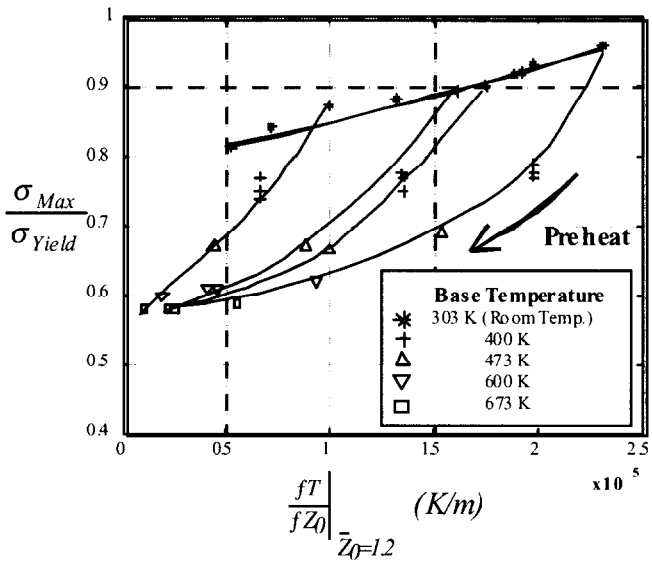

Figure 2.2. Relationship between maximum final stresses and process temperature gradient of 304 stainless steel for five different base temperatures.

By comparing the numerical results at different base temperatures, it is clear that uniform part preheating considerably reduces the residual stress. Some reduction of residual stress is due to reductions in strain mismatch, but most of the reductions due to preheating come from reducing the effective yield stress. The yield stress of SS304 decreases as the temperature increases, and by preheating the part, the maximum residual stress is limited by the maximum yield stress. The maximum reduction of residual stress by preheating the part is approximately 40% and achieved by preheating the part to 400°C. The final residual stress is after the part reaches the base temperature and the wall and base are cooled uniformly to room temperature.

Summary

Residual stresses during LENS fabrication can manifest themselves in two general ways. First the development and relaxation of residual stresses can lead to part distortion that can be rather significant especially in larger sections. Secondly residual stresses can affect part performance and may need to be considered in component design if a post processing stress relief is not employed. The holographic-hole drilling technique proved very successful in measuring residual stresses. In H-13, although the residual stresses were very low, it is known that considerable part distortion can occur during fabrication. Thus the distortion likely occurs during processing at elevated temperatures above the low temperature martensitic transformation which reduces the magnitude of the final stresses. In the case of austenitic stainless the measured residual stresses approached those of the yield stress in regions where high temperature gradients were developed.

The normalization technique developed to predict pool size, thermal gradients and finally residual stresses should help guide the engineer in selection process parameters that can minimize residual stresses. These calculations for example very effectively demonstrate the effectiveness of reducing residual stresses, The biggest pay-off in reducing residual stresses comes from uniform base plate preheating. The maximum reduction in residual stress that can result from this method is approximately 40% (from the yield stress) in 304 stainless steel wall builds. At large levels of base plate preheating, the reduction in residual stress is a very weak function of laser velocity and power. Thus at large levels of preheat, the full range of power and velocity can be used with minimal effects on maximum residual stress magnitudes. Finally, since preheating does not increase melt pool lengths significantly, any increase in melt pool size due to preheating can easily be eliminated by a small decrease in laser power or increase in laser velocity. In this way the process maps for melt pool length and temperature gradient discussed in Section 1 can be used together to suggest strategies for controlling residual stress magnitudes while still maintaining an optimal melt pool length.

It is clear that the development of residual stresses is complicated by the complex thermal excursions and are very dependent upon alloy metallurgical characteristics. Only through a detailed FEM approach can their development be better understood. Although this LDRD did not have an FEM component, the data developed here would be invaluable in validating any such predictions.

References

1. M. L. Griffith, M. E. Schlienger, L. D. Harwell, M. T. Ensz, D. L. Greene, J. E. Smugeresky, C. V. Robino, W. H. Hofmeister, M. J. Wert, D. V. Nelson, *Understanding Thermal Behavior in LENS Processing of Structural Materials*, Proceedings of The Mineral, Metals, and Materials Society Conference, March 3, 1999, (in press).
2. M. L. Griffith, M. E. Schlienger, L. D. Harwell, M. S. Oliver, M. D. Baldwin, M. T. Ensz, J. E. Smugeresky, M. Essien, J. Brooks, C. V. Robino, W. H. Hofmeister, M. J. Wert, D. V. Nelson, *Understanding Thermal Behavior in the LENS Process, Journal of Materials Design*, volume 20 number 2/3, June 1999, p 107-114.
3. A. Makino and D. V. Nelson, E. A Fuchs, D. R. Williams, *Determination of Biaxial Residual Stresses by Holographic-Hole Drilling Technique*, J. of Engineering Materials and Technology, Vol. 118, 1996, p.583.
4. A. Vasinonta, J. L. Beuth, M. L. Griffith, *Process Maps for Controlling Residual Stress and Melt Pool Size in Laser-based SFF Processes*, to be published in proceedings of the Solid Freeform Fabrication Symposium, August, 2000, Austin, TX.
5. A.Vasinonta, J. L. Beuth, M. L. Griffith, *A Process Map for Consistent Build Conditions in the Solid Freeform Fabrication of Thin-Walled Structures*, accepted to Journal of Manufacturing Science and Engineering, July 2000.

Section 3. Feeding of Multiple Powders and Transition Structures

The ability to produce graded microstructures and increase flexibility in alloy design will largely depend on the capability to feed multiple powders at independently controlled and variable rates. Improvements were made to powder feeders and delivery systems to minimize clogging and better control feed rates. However, the biggest advancement was the development of the capability to feed multiple powders at desired ratios to achieve a desired specific composition, and to transition through different ratios of individual powers. This has been accomplishes by using mass flow rate meters that can accurately deliver the desired mass of individual powders to the powder delivery nozzles feeding the laser melted pool.

The functionality of this newly developed capability was demonstrated using a number of powder combinations. One specific experiment designed to demonstrate the ability to feed multiple powders utilized two powders with vastly different densities: Ti-6Al-4V and a Ni-based superalloy IN 718. Powders were feed in a controlled (linear variation) manner from 100 % Ni alloy to 100% Ti alloy to produce a deposit 1 cm in diameter and 5 cm long. This sample was longitudinally sectioned and examined by optical microscopy as well as with SEM using EDS analysis, figure 3.1.

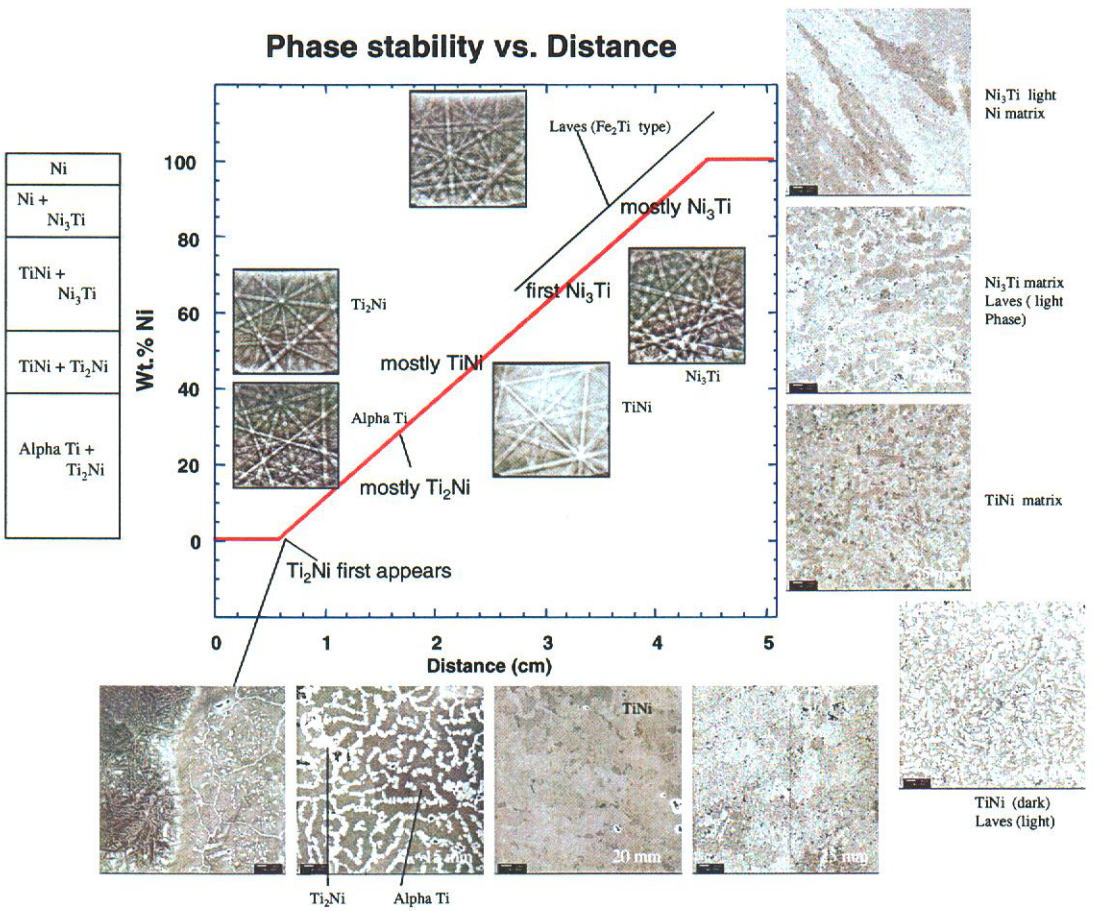

Figure 3.1. Results obtained from graded transition from Ti-6Al-4V and the Ni-based superalloy IN 718. Phases were identified by EDS and Kukuchi pattern orientation imaging.

A high degree of mixing within the liquid was achieved to give a uniform composition across the build although a number of phases were observed depending upon average composition. Analysis was conducted along the build to determine variation in compositions. Very good agreement was achieved between the target composition and that measured.

Results from the Ti-6Al-4V and Ni-based superalloy IN 718 are shown in figure 3.1. These are both complex alloys with a number of phases formed during solidification and cooling. The first powder fed was the Ti alloy with primarily an alpha Ti structure. With the addition of Ni alloy powder a second phase, Ti_2Ni identified by orientation imaging Kukuchi patterns and EDS analysis, also forms. It can be seen that different phases form as the composition changes. Although on a microscale a large variation in composition exists, on a bulk scale the Ni content changes in continuous manner as programmed by the two different feeders. These results were very encouraging and necessary for providing the ability of developing novel materials. This ability was used in designing alloys during other phases of the LDRD program.

Section 4. Microstructural Evolution During LENS Fabrication of H13 Tool Steel

Introduction

As discussed previously, the goals of the overall LENS research program were (1): to utilize the capabilities of LENS to build engineering structures that are difficult to produce with conventional processing and (2) to demonstrate the ability to develop integrated materials and process models that can be used to predict and tailor the properties of LENS engineered structures. This section describes one aspect of the program which is related to the second of these overall goals, and discusses the methodology required to analyze the development of microstructure in a complex alloy.

Approach

The approach used in the study incorporated four major parts: (1) Selection of an alloy system which represented a variety of important microstructural evolution features such as solidification segregation and solid state phase transformations; (2) Development of experimental techniques for measurement of thermal histories during fabrication (that can also be used for validation of process models); (3) Development of materials response models and experiments that describe the relevant microstructural changes for the alloy of interest; (4) Combination of the microstructural models and the process thermal histories (either experimental or model estimates) and comparison with the experimental microstructural and property measurements.

Selection of Alloy System

Given the wide variety of available alloys, their associated strengthening mechanisms, and the complexity of the LENS process, it is difficult to identify a single alloy system that represents all the possible mechanisms of microstructural evolution. However, as will be described below, one alloy type – tool steels – incorporates a significant variety of strengthening mechanisms and provides a suitable representation of a range of phenomena likely to be of importance in LENS processing. Moreover, tool steels are of major interest in rapid prototyping, so that the results of this work are directly applicable. A specific alloy of interest in this respect is H13, which is a hot work die steel often used for aluminum extrusion and casting dies.

H13 is a secondary hardening martensitic steel which is strengthened by both martensitic transformation and precipitation hardening. Thus, both diffusional (e.g. on-heating formation of austenite and precipitate formation) and non-diffusional (e.g. martensitic transformations) solid state transformations are important in this alloy, and must be accounted for in any description of microstructural evolution during processing. Moreover, the alloy contains

significant levels of substitutional alloying elements, which implies that solidification phenomena (e.g. solidification segregation and mode) may also be an important factor in the microstructural evolution.

The nominal composition of the powder used in this investigation is shown in Table 4.1. The alloy is seen to be a medium carbon steel, with principal alloying elements of Cr, Mo, and V. In the normal heat treatment condition (e.g. quenched and tempered), the microstructure consists of tempered martensite, with alloy carbides such as MC and M_2C distributed throughout

Table 4.1. Composition of H13 Tool Steel Powder.

Element	Concentration (wt%)
C	0.38
Mn	0.35
Si	1.0
Cr	5.52
Mo	1.61
V	0.87
P	0.009
S	0.18
Fe	bal

the matrix and along martensite lath boundaries [1]. In this condition the alloy generally displays an appropriate combination of strength and toughness for die applications [2]. The alloy is commercially available in powder form.

LENS Thermal Cycles

An experimental method for determining the thermal cycles associated with the LENS process was developed, and is shown in figure 4.1. In this arrangement, 0.13 mm diameter chromel/alumel thermocouples were inserted into the build at various locations along the z-axis, and were thus incorporated into the structure. Thermocouple data was collected at 100Hz. Both shell and block builds were monitored by this method, but the remainder of this section will discuss the results associated with the shell builds. The shells were 51 mm by 51 mm and were built using a matrix of processing parameters that included three power levels (200, 150 and 300 watts) and three travel speeds (5.9, 7.7, and 9.3 mm/sec). Typical thermal cycle results (for the 300 watt, 5.9 mm/sec condition) are shown in figure 4.2.

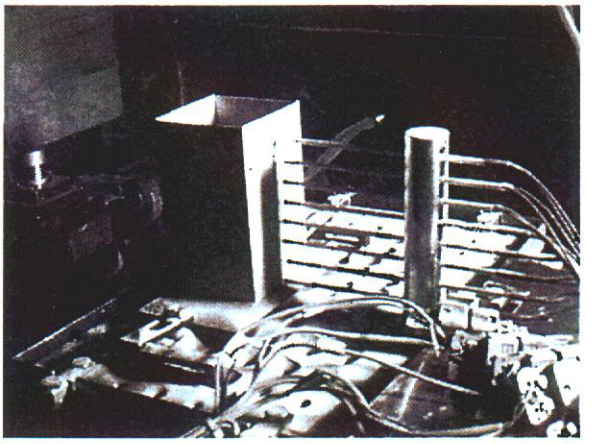

Figure 4.1. Photograph of experimental setup for thermocouple measurement of LENS thermal cycles in shell build.

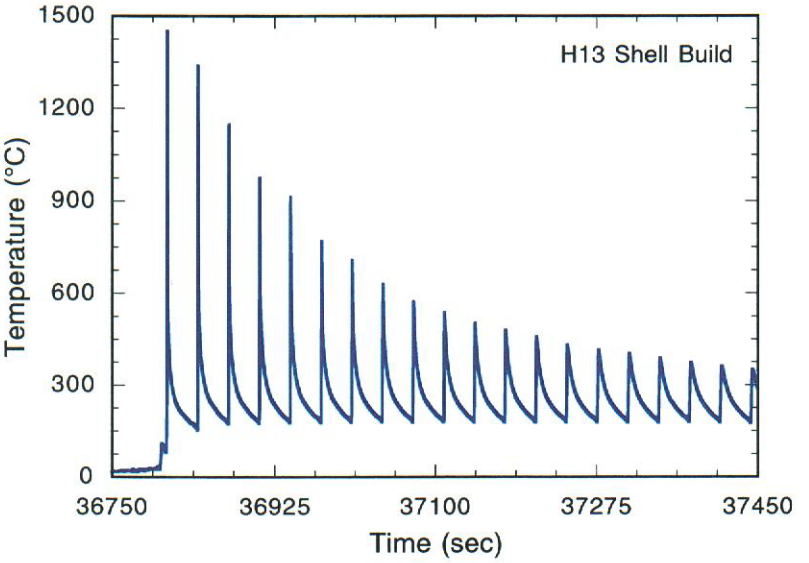

Figure 4.2. Measured thermal history for one location in H13 shell built at 5.9 mm/sec and 300 watts laser power.

The figure shows the thermal cycles experienced by one location within the part (at the center of a shell wall) and illustrates the complexity of the thermal history. The first peak in the history corresponds to the insertion of the thermocouple, and represents the first melting cycle and cooling of the molten pool. The subsequent thermal cycles, occurring every 33 seconds as the next layer is deposited, correspond to the thermal exposure of the underlying passes. Results are shown for 20 cycles, or build passes, where it can be seen that peak temperatures decrease monotonically with each succeeding pass. In the first (deposition)

pass the maximum cooling rate is ~$5x10^3$°C/sec. With these shell builds little heat is accumulated in the part, so that the interpass temperature remains essentially constant at ~150°C. Thermal predictions were attempted using Rosenthal analytical solutions [3] as well as with FEM using element birthing techniques. However, as has been demonstrated for weld process models [4,5] experimental data such as that shown in figure 1b is critical for model validation. In this study the experimental data, rather than a thermal model, was used for microstructural predictions. However, it must be noted that for true "processing for properties" a validated thermal model is required.

Qualitative Interpretation of Microstructure Evolution

The effect of the thermal history on the microstructure of H13 LENS build can be qualitatively understood with reference to figure 4.3. The figure shows the microstructure of a shell near the top of the build, and indicates the relationships between the thermal cycles, microstructure, and the phase diagram for H13 tool steel. In essence, then, the micrograph of figure 4.3 can be viewed as a snapshot of the various stages of micrstructural evolution in the build. For example, the uppermost layer of the build has experienced only a single thermal cycle, while the second layer has experienced the first two cycles shown in figure 4.3, and the third layer has experienced the first three, *etc*. The microstructure can be divided into three regions that correspond to the peak temperature of the most recent thermal cycle experienced at that location. Relative to the phase diagram, these regions correspond to: Region I, supercritical-melting-solidification (*i.e.* heating above the austenite solvus at approximately 940°C); Region II, intercritical heating (*i.e.* in the two-phase austenite plus

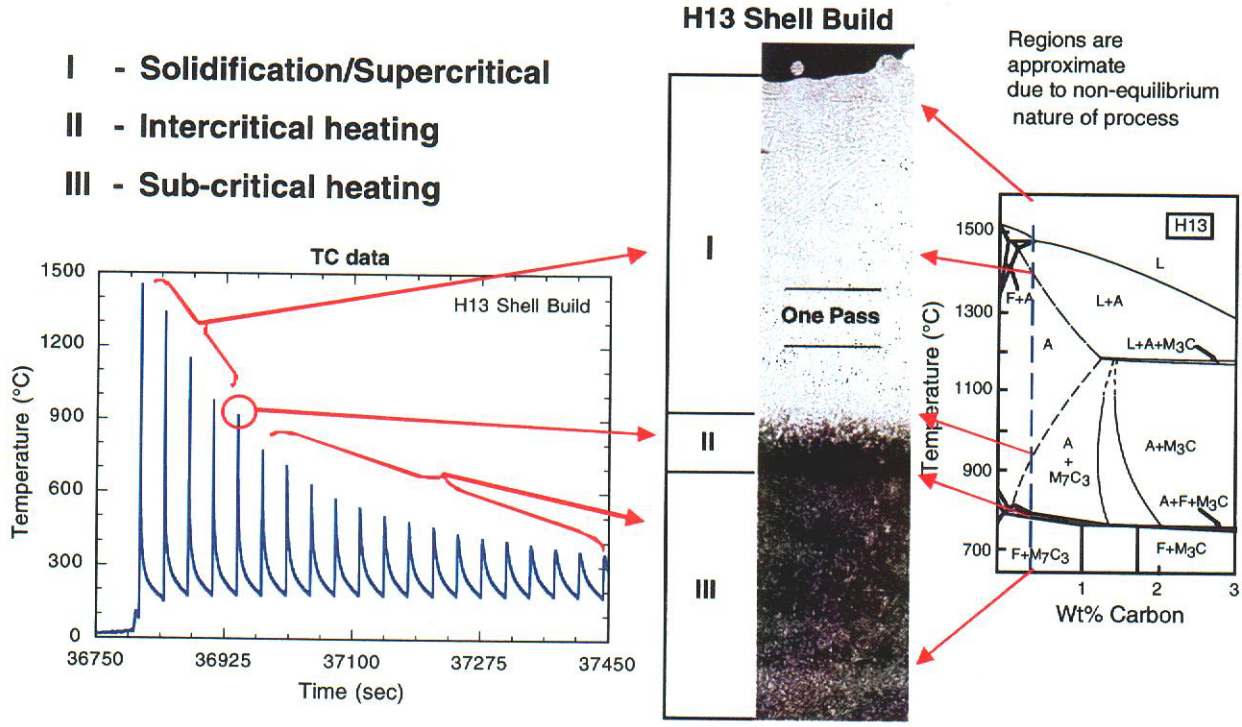

Figure 4.3. Optical micrograph of top edge of H13 shell build in relation to thermal cycles and H13 phase diagram. The height of one build pass is also shown on the micrograph and is approximately 0.25 mm.

carbide region between 800 and 940°C); Region III, subcritical heating (*i.e.* to temperatures below the start of austenite formation at 800°C).

Region I consists of material which is either melted, partially melted, or heated into the fully austenitic portion of the phase diagram. Given the high hardenability of H13, the microstructure in this region would be expected to consist essentially of untempered martensite that is formed on cooling from the austenitic temperature range (the martensite start temperature for H13 occurs near 350°C). For the thermal history shown in figure 4.3, four passes, including the final deposition pass, are within this region.

Region II consists of material heated into the intercritical temperature range where austenite and M_7C_3 carbides are the dominant stable phases. For the thermal history shown in figure 4.3, only one pass is within this region and it was heated into this region during deposition of the final pass. Microstructural changes within this region are dramatic, and range from essentially 100% martensite (which was 100% austenite at temperature) to martensite plus carbide near the lower extreme of the region. The kinetics of the decomposition in this Region (from a fully martensitic structure after the second to last pass to the gradient structure after the last pass) is extremely rapid and occurs entirely during the one thermal cycle. It is interesting that the height of this region is close to that of a single pass height, and based on the phase diagram, would have contained a thermal gradient of ~150°/0.25 mm (~600°C/mm).

Region III consists of material which has experienced the supercritical and intercritical thermal cycles, as well as numerous subcritical cycles. These subcritical cycles can be expected to further temper (overage) the microstructure and are likely to result in additional softening. The final microstructure in the bulk of the build consists of tempered martensite with a bimodal distribution of fine V (A areas) and larger Cr (B areas) containing carbides as shown in figure 4.4.

In subsequent subsections, the microstructural evolution in each of these regions will be examined in more quantitative detail. The regions are discussed in order of increasing complexity, with the supercritical and subcritical regions discussed first followed by a consideration of the intercritically heated region.

Microstructure Evolution in the Supercritical Region

The first thermal cycle experienced by material in Region I is the pass which the alloy is deposited by the LENS process. In this pass the microstructural evolution is dominated by two events, the alloy solidification and the subsequent transformation to martensite on cooling. The microstructure of the final pass is shown in figure 4.5, and appears to consist essentially of untempered martensite. The hardness of this pass was observed to be near 55 HRC, which is consistent with that of untempered martensite in this alloy.

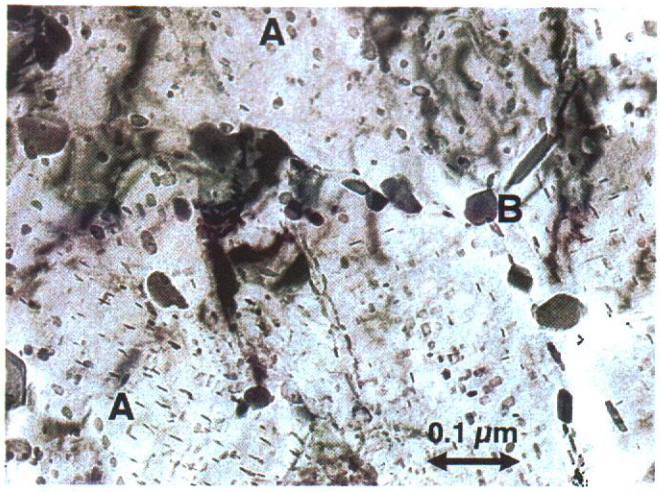

Figure 4.4. TEM image of H13 LENS deposit showing bimodal distribution of carbides. A and B denote typical regions of V and Cr rich carbides, respectively.

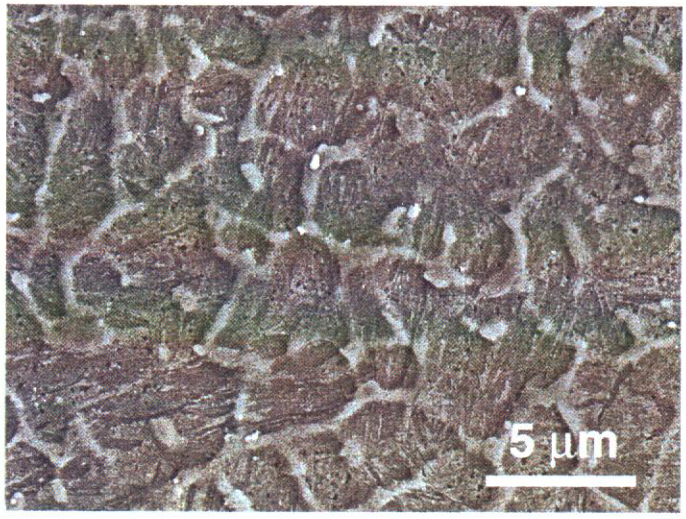

Figure 4.5. Microstructure of last pass of H13 shell build.

Figure 4.5 suggests that there is some interdendritic segregation in the last pass which is consistent with low diffusion rates of substitutional elements during austenite solidification [6]. Microprobe measured segregation ratios (interdendritic boundaries)/(dendrite cores) were: Cr= 1.3, Mo = 1.2, and V= 1.5. Because of the higher concentration of alloying elements in the interdendritic areas it is also possible that some alloy carbides are formed on cooling, although none were detected in TEM. Homogenization estimates for the substitutional alloying elements are strongly dependent on the actual peak temperature reached during the subsequent supercritical heating cycles. However, due to the sluggish

diffusion kinetics in austenite and short diffusion times, this solidification induced segregation is not significantly reduced. On the other hand, diffusion estimates for interstitial carbon, [7] that considered the length scales involved (approximately 3-5 μm) indicated that the carbon is easily homogenized during the subsequent supercritical heating cycles. Hardness profiles across Region I were effectively constant at a value of approximately 55 HRC, so that both the microstructure and properties of Region I are consistent with untempered martensite.

The microstructural evolution in Region I, though physically complex, is comparatively simple to describe quantitatively. The deposition pass solidifies with some solidification segregation, but is cooled sufficiently rapid for martensite to form (even in the 2-dimensional heat flow condition of the shell configuration). During subsequent reheating cycles with peak temperatures above about 940°C, the alloy is repeatedly reaustenitized and quenched back to untempered martensite. In the current study, these processes were not modeled explicitly because the microstructural result, untempered martensite, can easily be predicted from a knowledge of the peak temperature of the thermal cycle. Obviously, for materials with lower hardenability such a prediction may not be as straightforward, but models are available for cases where other transformation products would be expected at these cooling rates.

Microstructure Evolution in the Subcritical Region

Although the starting microstructure for thermal cycles in the subcritical region are those which result from the intercritical thermal cycle, it is appropriate to discuss the subcritically heated region first. This is because, as will be discussed later, the metallurgical processes in the intercritical region are extremely complex and affected by the very steep thermal gradients within the intercritically heated region. At this point it is sufficient to consider that the microstructure of the alloy following the intercritical thermal cycle basically consists of a structure which is similar to tempered martensite (recovered martensite with alloy carbides distributed within the martensite laths, along lath boundaries, and along grain boundaries). With this assumption, it is reasonable to conclude that the principal microstructural change that occurs during the subcritical cycles is essentially aging (growth) of the carbides.

H13 Aging Model A description of the overaging process in the H13 requires a numerical model that can be applied to the rapid thermal cycles associated with the LENS process. In this section a simple kinetic parameter is defined which relates hardness to thermal history. The model is based on classical coarsening models, and the additivity rule is used to apply the model to LENS thermal cycles. In the model development, a kinetic parameter that is simply related to hardness is defined first.

It is assumed that hardness is proportional to shear strength, and that the analysis for the strengthening effect of incoherent precipitates [8] applies,

$$H \propto \tau = \frac{\alpha \mu b}{\lambda} \qquad [1]$$

where H is the hardness, τ is the shear strength, α is a geometric factor, μ is the shear modulus, b is the burgers vector, and λ is the interparticle spacing. For overaging, the volume fraction of precipitates is assumed constant so that $\lambda \propto r$, where r is the radius of precipitates (assumed to be spherical). Thus, in the overaging regime, the following microstructural relationship is obtained:

$$H \propto \frac{1}{r}. \qquad [2]$$

During aging, the precipitates are assumed to follow classical coarsening kinetics [8] (*i.e.* Lifshitz and V. V. Slysov [9] and Wagner [10] or LSW kinetics), so that

$$\bar{r}_t^3 = \bar{r}_0^3 + Kt, \qquad [3]$$

where $\bar{r}_0$ is the mean initial particle radius and $\bar{r}_t$ is the particle radius at time t. The coefficient K in Equation 3 is generally given by an equation of the form

$$K = \frac{8}{9}\frac{D\sigma V_m C_\alpha(\infty)}{RT} f(\phi), \qquad [4]$$

where D is the diffusivity, σ is the interfacial energy, V_m is the molar volume of precipitate, $C_\alpha(\infty)$ is the solubility of the solute, R is the ideal gas constant, T is the temperature, and $f(\phi)$ is a function which depends on the particular coarsening theory ($f(\phi) = 1$ for the LSW theory). If it is assumed that all factors other than diffusivity are independent of temperature, and that the temperature dependence of D can be represented by $D = D_0\exp(-Q/RT)$, then Equation 4 can be written as

$$K = K_1 \frac{\exp\left(\frac{-Q}{RT}\right)}{T}, \qquad [5]$$

where K_1 is a constant. Combination of Equations 3 and 5 yields an expression for the coarsening rate as a function of time and temperature:

$$\bar{r}_t^3 = \bar{r}_0^3 + K_1 \frac{\exp\left(\frac{-Q}{RT}\right)}{T} t. \qquad [6]$$

Substitution of Equation 6 into Equation 2 (with $\bar{r}_t = r$) and rearranging leads to the result

$$H \propto K_2, \qquad [7]$$

where K_2 has the form

$$K_2 = \left(\bar{r}_0^3 + \frac{K_1 t \exp\left(\frac{-Q}{RT}\right)}{T} \right)^{-1/3}. \qquad [8]$$

Thus, a plot of H versus K_2 should be linear. The most direct means to apply this methodology is to search for values of $\bar{r}_0$, K_1, and Q that maximize the linearity of the plot. This can easily be accomplished in a spreadsheet application. Alternatively, if values for any of the parameters are known, such as an initial size or the activation energy for the diffusion of the rate limiting precipitating species, these can be used to reduce the number of fit parameters.

Isothermal aging experiments were conducted on single-line LENS deposits to determine the model fit parameters. The single line deposits were made using parameters within the range used for the shell builds, and were deposited on 6mm thick plates of wrought H13. The hardness for different times and temperatures measured on these samples is shown in figure 4.6a. The results from the procedure described above to fit this data (Equations 7 and 8) are shown in figure 4.6b. The optimized fit parameters for this data set are $\bar{r}_0 = 3.99 \times 10^{-7}$, $K_1 = 0.04048$, and $Q/R = 38143$, and the hardness for any isothermal heat treatment can be represented by a line of the form

$$KHN = 285.31 + 1.495 \times 10^{-4}(K_2) \qquad r^2 = 0.9957. \qquad [9]$$

These parameters linearize the data over a wide range of aging conditions, including those conditions near peak hardening and overaged. The apparent activation energy for the softening, 75,790 cal/mole, is higher than might be expected for coarsening of alloy carbides in H13. For example, the activation energy for the diffusion of Mo in ferrite is given [11] as 57,700-60,000 cal/mole (the diffusion of Cr would be expected to have a similar activation energy). However, given the assumptions inherent in the model, such as spherical precipitates, *etc.*, this discrepancy is not thought to be a major drawback with respect to the application of the model.

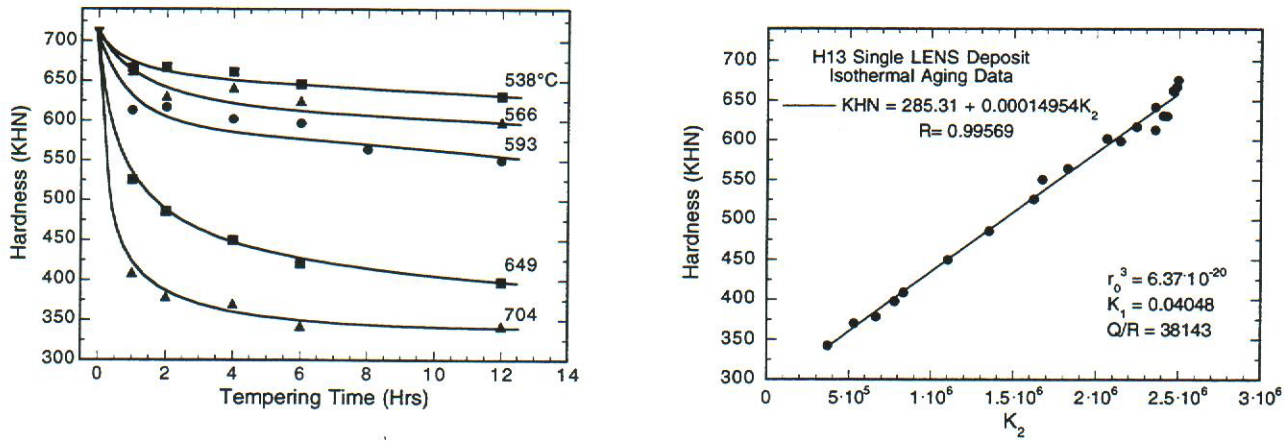

(a) (b)

Figure 4.6 (a) Isothermal aging data for single line LENS deposits. (b) Correlation of data in (a) using Equations 7 and 8.

Application to LENS Thermal Cycles Application of the overaging model to LENS deposits requires a means to estimate the cumulative effect of the thermal cycle on the kinetics. A common approach for estimating this effect is the additivity principle [12,13]. To apply the additivity principle, a thermal cycle is modeled as a series of small isothermal steps. At each step, the time elapsed is a fraction of the time required, at that temperature, to achieve a given amount of transformation or hardness. When these fractions sum to unity, the given hardness has been achieved. Formally, this can be written as

$$\int_0^t \frac{dt}{t_a(T)} = 1, \qquad [10]$$

where t is the time and $t_a(T)$ is the time to reach the given hardness isothermally. For discrete time steps, Equation 10 can be written in the summation form, or

$$\sum_0^t \frac{\Delta t}{t_a(T)} = 1. \qquad [11]$$

From Equation 9, $H = H_0 + mK_2$, where H_0 and m are the intercept and slope of the fit to the isothermal aging data, respectively, it is apparent that

$$H = H_0 + m\left(\bar{r}_0^3 + \frac{K_1 t \exp\left(\frac{-Q}{RT}\right)}{T}\right)^{-1/3} \qquad [12]$$

or, upon rearranging,

$$t = t_a(T) = \frac{T\left[\left(\frac{m}{H - H_o}\right)^3 - \bar{r}_0^3\right]}{K_1 \exp\left(\frac{-Q}{RT}\right)}. \qquad [13]$$

For an isothermal hold, Equation 13 represents the time required to reach a given hardness, H, at a given temperature, T. Using a series of small isothermal steps to represent a thermal cycle, the summation of Equation 11 can be solved by using a goal seeking routine to find the hardness that satisfies the summation for that thermal cycle. Alternatively, the summation can be solved sequentially by calculating the softening during a given time step, adjusting the temperature to the temperature associated with the next time step and adjusting the start time to that which it would have been had the temperature always been at the new temperature, and iterating this procedure over the entire thermal cycle.

Microstructure Evolution in the Intercritical Region

With respect to microstructural evolution, the region of the build that is heated to peak temperatures in the intercritical temperature range is perhaps the most complex. This complexity is due to the fact that the microstructural changes are rapid, dramatic, and are not, as is the case for the supercritically heated region, reversed by solid state transformations on cooling. The rapidity of the reactions is illustrated by the high speed dilatometry results for H13 shown in figure 4.7. At a heating rate of 100°C/sec, the lower critical temperature (start of austenite formation), A_{c1}, occurs at approximately 860°C while the upper critical temperature (completion of austenite formation), A_{c3}, occurs at approximately 960°C. Thus, the entire transformation spans about 100°C, or 1 second in time. From a starting microstructure of untempered martensite, the phase diagram of figure 4.3 indicates that the first phase to form would be austenite and this would be expected to nucleate along the prior austenite boundaries within the martensite. However, depending on the heating rate, carbides might also be expected to form before as well as after the lower critical temperature is reached. In essence, therefore, the microstructural evolution in the intercritically heated region consists initially of the nucleation and growth of both austenite and carbide. As the upper critical temperature is approached, the carbides formed at lower temperatures within the intercritical region progressively dissolve until they are completely consumed at the upper critical temperature.

With respect to development of mechanical properties, the importance of the intercritical heating can be understood with reference to figure 4.8. The figure shows microhardness profiles for

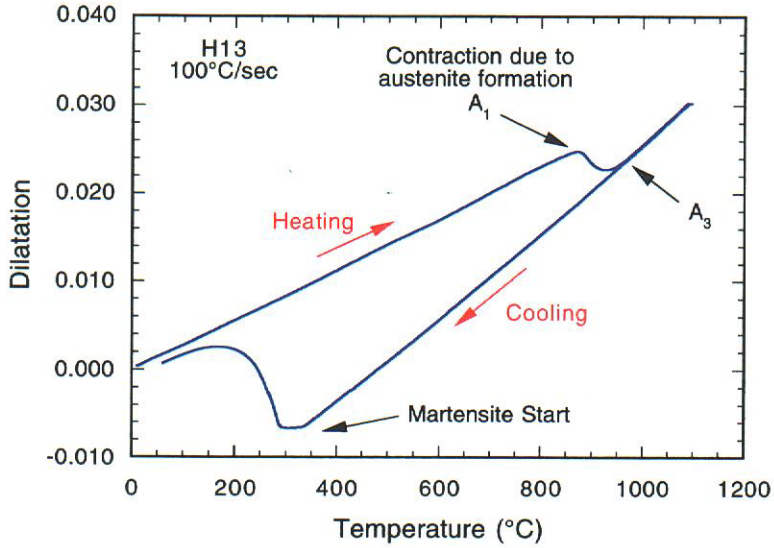

Figure 4.7. Gleeble dilatometry results for H13 steel heated at 100°C/sec.

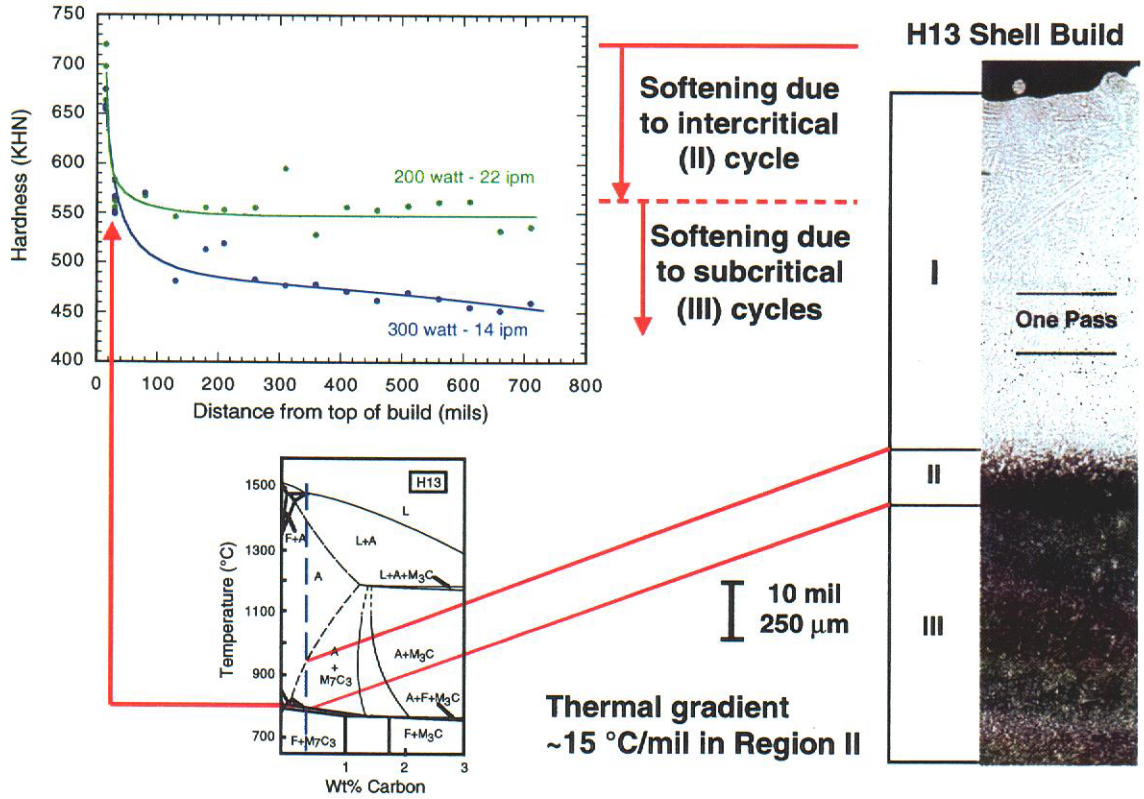

Figure 4.8. Diagram showing relationships between hardness and various heating regions.

the highest and lowest heat input conditions starting at the top layer of the shell build and progressing toward the bottom of the build. As shown, for the low heat conditions, essentially all of the softening occurs during the intercritical thermal cycle. For the high heat input conditions, most of the softening occurs during the intercritical cycle, but there is some additional softening during the subsequent subcritical cycling.

The complex series of microstructural changes which occur at temperatures in the intercritical region were not modeled explicitly in the current work. From a kinetic perspective, however, it is reasonable to conclude that the softening that occurs at lower temperatures within the intercritical region is similar to that which occurs in the subcritical region, and is due to the rapid precipitation and diffusional growth of carbides. At high temperatures within the intercritical region, a nearly fully austenitic structure is developed at the peak temperature, so that the upper portion of the region is similar to the supercritical region, and reverts to martensite on cooling. Thus, in the current study, the intercritical region was simply modeled by using the same approach described for the subcritical region. It is fully recognized that this approach does not completely describe the microstructural evolution in the intercritical region, but, as will be seen below, the general trends in softening response are captured. Moreover, it will be seen that the precision of the measured thermal cycles is not sufficient to warrant a more detailed model of the microstructural evolution in the intercritical region.

Model Predictions *vs.* Experiments

The microhardness tests conducted on the shell builds showed that the hardness of the supercritical region was the same for all processing parameters and was consistent with that of untempered martensite. The hardness dropped rapidly in the region of the first intercritical pass and then decreased to greater or lesser degrees depending on heat input. For example it was found that the highest hardness build corresponded to the lowest heat input deposit (200 watts and 9.3 mm/s) and the softest deposit corresponded to the highest heat input deposit (300 watts, 5.9 mm/s). This behavior is shown in figure 4.9a, where the hardness is plotted as a function of distance from the last pass for these two process conditions, along with model predictions based on the measured thermal cycles. The hardness changes are consistent with the model predictions shown in figure 4.9a. As a result of the rapid softening kinetics and its exponential temperature dependence, the calculated hardness is primarily controlled by the peak temperature of the thermal cycle within the intercritical temperature region. The measured peak temperature of the intercritical pass of the high heat input build was higher than that of intercritical pass of the lower heat input build, and this accounts for the differences in the predicted initial hardness drop for the two sets of parameters. Subsequent tempering passes are of similar duration as the first tempering pass, but at progressively lower temperature resulting in little additional tempering.

The model predictions in figure 4.9b were determined with the aging model and show that hardness strongly depends on the peak temperature of the single thermal cycle within the intercritical region. For a region that experiences a peak temperature of 800°C, the hardness drops from ~710 KHN (that of untempered martensite) to ~645 KHN. For a peak

temperature of 925°C, the hardness drops to ~515 KHN. The tempering response, or predicted hardness is, however, much more complex. It must be remembered that a thermal gradient is associated with

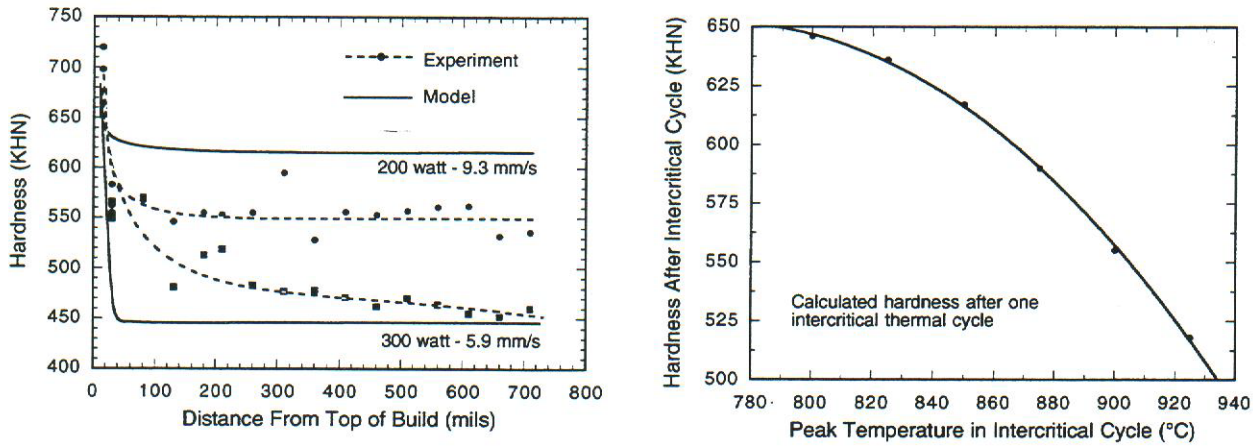

(a) (b)

Figure 4.9. (a) Comparison of measured and predicted hardness distributions in LENS H13 wall build. (b) Plot of calculated hardness as a function of peak temperature within the intercritical temperature range.

the peak temperature of each tempering pass. All the temperatures within the intercritical and upper subcritical regions will correspond to the peak temperatures at some specific point, or line along the build. Furthermore, the height of the passes are on the order of the intercritical zone of the first tempering pass. Thus one would expect that a hardness gradient should exist within individual passes. Also, there could be regions further down the build that would be harder than regions closer to the top. This was actually observed, and accounts for some of the scatter in the data shown in figure 4.9a and the banded etching behavior of the microstructure, figure 4.3. To average some of the localized variation, each hardness value plotted in Figure 4.9a is actually the average of three measurements made along a line at the same distance from the top of the build.

The temperature cycles used in the calculations were those experimentally measured with thermocouples. Although these thermocouples are small (0.13 mm diameter), they are still one half the height of the individual build passes. As shown in the microstructure of figure 4.3, in the intercritical region the thermocouples lie within a temperature gradient of ~600°C/mm and therefore provide some average temperature within the temperature gradient (note that the placement of individual wires of the thermocouple further degrades this spatial resolution). Thus, the uncertainty in temperature at a specific location is a minimum of (600°C/mm)(0.13 mm) ≈ 80°C. It is therefore not possible to ascribe differences between the measured and predicted hardness to deficiencies in the model alone. Moreover, the uncertainty in measured temperature cycle would preclude validation of a more detailed description of the microstructural evolution in the intercritical region. As a result, development of such a detailed model of the intercritical heating was not attempted.

Nevertheless, the peak temperatures measured with the thermocouples, coupled with the simple model, resulted in a correct prediction of the softening trends, figure 4.9a. The differences in softening for the two heat inputs is probably result of the thermal gradient being flatter in the high power/low speed build than in the low power/high speed build, rather than the thermal couple placement. In general it has been found that hardness correlates better with travel speed than with laser power [14]. Thus, it can be seen that the details of the hardness and tempering kinetics are highly dependent upon the height of the individual build passes, as well as the thermal gradient in the intercritical region of the first tempering pass.

H-13, as noted earlier, is a medium carbon tool that is secondary hardened by alloy carbides. Thus, on aging, the yield strength is increased by the precipitation of carbides but the hardness and ultimate strength decreases due to tempering with the reduction of carbon in the martensite. In our analysis we have related hardness to the flow stress. It is generally agreed that the hardness is best correlated with flow stress at ~ 8% strain and not with that of the 0.2% yield strength. Figure 4.10 shows tensile results for the nine build conditions, three power levels and three transverse speeds. The 0.2% yield strength, ultimate tensile strength and strain to failure are shown for power levels of 200, 250 and 300 W and 5.9, 7.6 and 9.3 mm/s (14,18 and 22 ipm). It can be seen that the yield strengths are the highest and the ultimate the lowest for the lowest travel speed of 14 imp. The trend in ultimate tensile strength is consistent with the hardness behavior in which hardness decreased with decreasing travel speed. This correlation would be expected since the strains to failure are ~ 6%. There are several exceptions in this behavior in the data in figure 4.10, especially the lower than expected UTS of the build at 200 W and 22 ipm. However, this is likely a result of porosity and possibly some lack of fusion defects which are more likely at low power levels and high transverse speeds and that is reflected in the low strain to failure. In this case the ultimate strength is actually a reflection of defects rather than the material property.

It is intriguing from a design standpoint that the material properties of the LENS samples can be very advantageous. The outer surface layers of all the LENS deposits have a very high hardness, that of untempered martensite, while the interior of the build can be designed with higher yield strength and improved toughness. There are a number of Sandia components where these characteristics would be desirable.

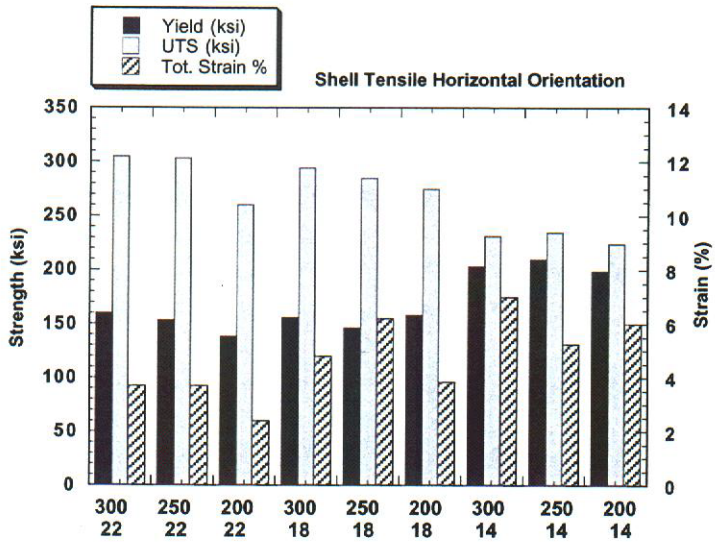

Figure 4.10. Tensile results showing 0.2% YS, UTS, and strain to failure of shell builds for nine process conditions: 200, 250 and 300 watts and 14, 18 and 22 ipm.

Summary

In this work H13 tool steel was used as a model system to examine the requirements associated with application of LENS as a processing for properties tool. H13 was selected because it exhibits a number of representative microstructural features as well as its industrial importance. Development of the LENS process to its full potential requires the development of suitable process and materials models as well as integration of the two, and these were attempted for H13 LENS shell builds. It was found that application of this approach is complex, but for H13 the microstructural development can be divided into three regimes that make the prediction of the overall microstructural evolution more tractable. Two major difficulties were encountered. First, the steep thermal gradients associated with the process make extremely accurate descriptions of the thermal environment, whether experimental or numerical, an absolute requirement for accurate microstructural models. The level of accuracy required in these thermal descriptions may, however be very difficult to achieve. Second, the microstructural evolution in the intercritical region is very rapid and is only qualitatively understood. Additional work in this area is needed, but will only be of value if precise thermal descriptions are also available. Nevertheless, the combination of simple microstructural models with experimental descriptions of the thermal history yielded reasonable estimates of the microstructural evolution, and demonstrate the feasibility of the approach. A variation of this section has been published in the open literature [15].

References

1. P. W. Hochanadel, Colorado School of Mines PhD Dissertation T-4775, (1996).
2. Carpenter Technology Corporation Product Literature, No. 883 Tool Steel, (1988).
3. D. Rosenthal, *Trans ASME*, Nov (1946), pp. 849-866.
4. J. Dike, C. Cadden, R. Corderman, C. Schultz and M. McAninch, *Trends in Welding Research, Proc. 4th International Conference*, Eds. Smart, Johnson and David, ASM, (1996), pp. 57-65.
5. J. J. Dike, J. A. Brooks, J. S. Krafcik, *Trends in Welding Research, Proc. 4th International Conference*, Eds. Smart, Johnson and David, ASM, (1996), pp.159-164.
6. J. A. Brooks, M.I. Baskes and F. A. Greulich, Metall. Trans. A, Vol.22A (1991), pp. 915-926.
7. J. N. Dupont, C. V. Robino, and A. R. Marder, *Acta Materiallia*, Vol. 46, (1998), pp. 4781-4790.
8. R. E. Smallman, *Modern Physical Metallurgy, - Fourth Edition*, Butterworths, London, (1985), pp. 394-407.
9. I. M. Lifshitz and V. V. Slyozov, *J. Phys. Chem. Solids*, Vol. 19, (1961), pp. 35-50.
10. C. Wagner, Z. Elektrochem., Vol. 65, (1961), pp. 581-591.
11. E. A. Brandes, *Smithells Metals Reference Book Sixth Edition*, Butterworths, London, (1983), p. 13–64.
12. E. Scheil, *Archiv. fur Eisenhuttenwesen*, Vol. 12, (1935), pp. 565-567.
13. J. W. Christian, *The Theory of Phase Transformations in Metals and Alloys Part I*, Pergamon Press, New York, (1981), pp. 542-548.
14. M. Griffith, E. Schlinger, L. Harwell, M. Oliver, M. Baldwin, M. Ensz, J. Brooks, C. Robino, J. Smugeresky, W. Hofmeister, M. Wert, and D. Nelson, *Materials and Design*, Vol. 20, Elsevier Science Ltd, (1999), pp. 107-213.
15. J. Brooks, C. Robino, T. Headley, S. Goods, M. Griffith, *Solid Freeform Fabrication Symposium 1999*, Ed. D. Bourell, J. Beaman, R. Crawford, H. Marcus and J. Barlow, U. of Texas at Austin, (1999) pp. 375-382.

Section 5. Aging Response of 17-4 PH Martensitic Stainless Steel LENS Deposits

The results from the H13 tool steel study, Section 4, indicated that the as-deposited condition for that alloy can be characterized by essentially two regions, an untempered martensite in the last several layers and an overaged (over tempered) structure in the interior. This dual microstructure may be desirable for some LENS applications, but in others, a full heat treatment (austenitization, quench, and temper) may be required to develop appropriate properties. This complex microstructure is a consequence of two principal features of the H13 alloy; the aging kinetics and the solid state transformation behavior. Carbon diffuses rapidly in steels, and as a result, the kinetics of precipitation are relatively rapid in the subcritically heated region of deposits. Moreover, it was seen that in the intercritically heated region of LENS builds, the formation of carbides (a principal hardening constituent) is an integral part of the formation of austenite. Carbide formation is extremely rapid and, in effect, develops an overaged-like microstructure during a single thermal cycle. As a result of these observations, a limited study was directed at determining whether this response was typical of the LENS deposits in precipitation strengthened steels, or whether it was a consequence of the H13 alloy characteristics. For this study a steel with significantly slower precipitation kinetics and different on-heating transformation behavior was used. The alloy selected was 17-4 PH, which is a precipitation strengthened martensitic stainless steel. This alloy is strengthened by the precipitation of Cu, in which the formation of austenite is not integrally linked to the precipitate formation.

Experimental

For the experimental trials, commercial 17-4 powder was used with the composition shown in Table 5.1.

Table 5.1 Composition of 17-4 Powder.

Element	Concentration (wt%)
C	0.054
Mn	0.53
Si	0.51
Cr	15.35
Ni	4.59
Cu	3.18
Nb	0.27
Mo	0.20

LENS block builds, figure 1.1, were fabricated using process parameters of 520 W – 40 ipm - 30 gpm powder feed rate and 700 W - 80 ipm - 36 gpm, and shell builds with 330 W - 20 ipm – 20 gpm and 520 W - 40 ipm - 30 gpm. Heat treatment studies of the block builds included direct aging at temperatures in the range of 400 to 550°C for 4 hr. Separate test samples were also exposed to full heat treatments that included a solution heat treatment at 1038°C for 1 hr followed by air cooling. Aging of the solution heat treated samples was conducted at either 400 or 450°C for 4 hr. Property analysis included hardness and tensile tests. SEM analysis was used for assessment of the fracture behavior.

Results and Discussion

The results of the direct aging study are summarized in figure 5.1. The as-deposited hardness for the builds is in the range of about 30-32 HRC, and is similar to that for wrought 17-4 in the solution treated condition (AMS 5604D, [Ref. 5.1], specifies a hardness of not greater than 38 HRC in the solution heat treated condition). Direct aging for 4 hrs results in a classical precipitation hardening response, with peak hardening occurring at temperatures near 450°C.

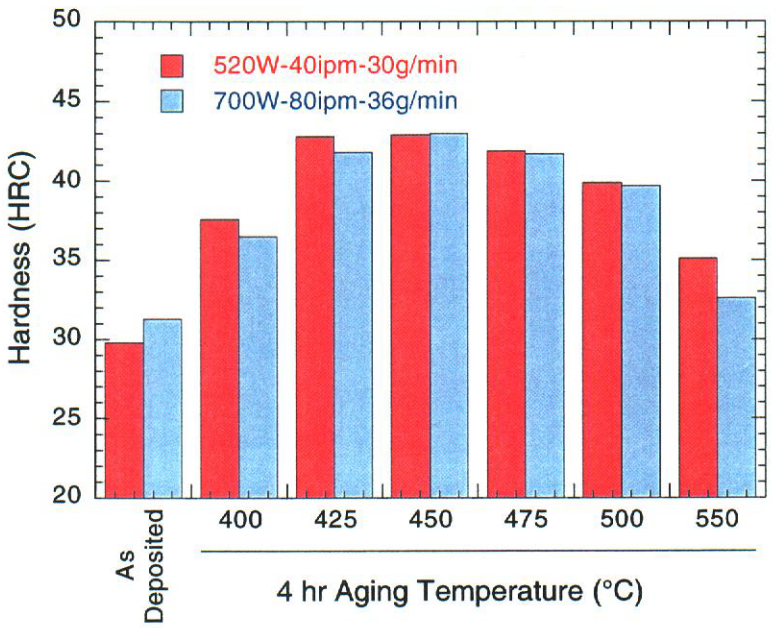

Figure 5.1. Hardness of 17-4 LENS block builds as deposited and after direct aging heat treatments for 4 hr.

There is no obvious or significant effect of process parameters, which support the conclusion that blocks deposited under both conditions were effectively in the solution heat treated condition. Although direct comparisons cannot be made with specification requirements for

wrought 17-4 PH, AMS 5604D [5.1] specifies a hardness in the range of 38 to 45 following aging at 496°C for 4 hr, and a hardness of 35 to 42 following aging at 551°C for 4 hr. Therefore, the hardness following aging at 500°C falls well within these requirements while the hardness after aging at 550°C is just short of meeting the specification. Taken together, the observations concerning as-deposited hardness, aging response, and similarity to the wrought alloy indicate that the 17-4 PH alloy composition can be LENS deposited in an essentially solution treated condition. Although no detailed microstructural characterization was conducted, it is believed that, in comparison to the H13 tool steel, this is a consequence of the slower precipitation kinetics and more reversible austenite formation behavior in the17-4 alloy system.

As a further evaluation of the heat treatment response of the LENS builds, solution heat treatment coupled with aging trials were conducted. The results of these trials are shown in figure 5.2, which shows the hardness after solution heat treatment as well as solution heat treatment and aging. Relative to the as-deposited condition, the solution heat treatment has virtually no effect on the hardness of the builds, which further substantiates the conclusion that the as-deposited microstructure is effectively solution treated. In addition, the aging response of the solution treated builds is similar to the direct aging trials. The response of the two LENS processing conditions is again similar and indicates that the alloy is relatively insensitive to processing conditions over the range examined.

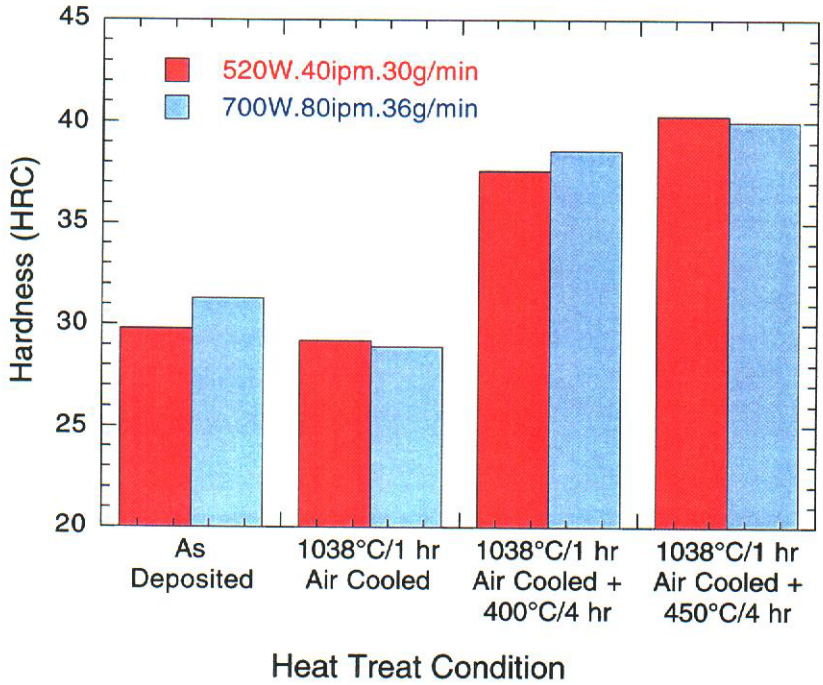

Figure 5.2. Hardness of 17-4 LENS block builds as deposited, after solution heat treatment, and after aging for 4 hr.

Tensile tests were conducted on the LENS builds in several heat treatment conditions, but displayed strength and ductility values that were significantly below typical values for the wrought alloy in the same condition. Fractography, figure 5.3a, indicated that the builds contained excessive porosity and is believed to be the cause of the poor tensile response. Examination of the fracture surfaces away from the voids, figure 5.3b, showed that failure occurred by microvoid coalescence, and is typical of the 17-4 alloy. The large porosity fractions present in the 17-4 builds is problematic and is discussed in more detail in Section 8 of this report, but appears to be related to the porosity in the starting powder. It is believed that suitable control of the starting powder would preclude development of porosity in the 17-4 LENS builds.

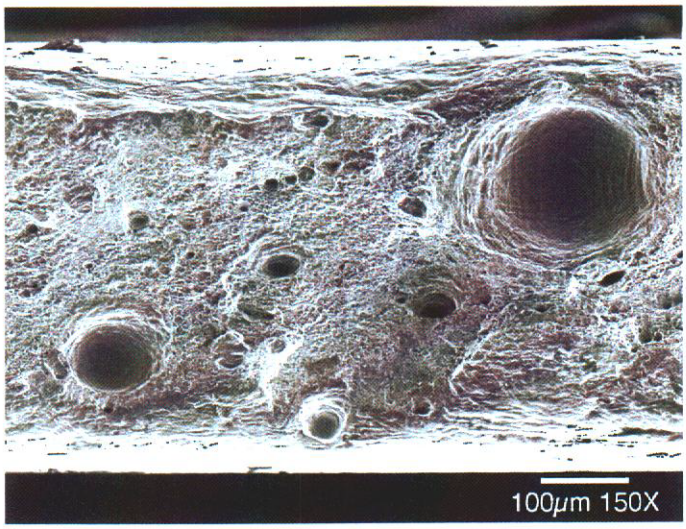

(a)

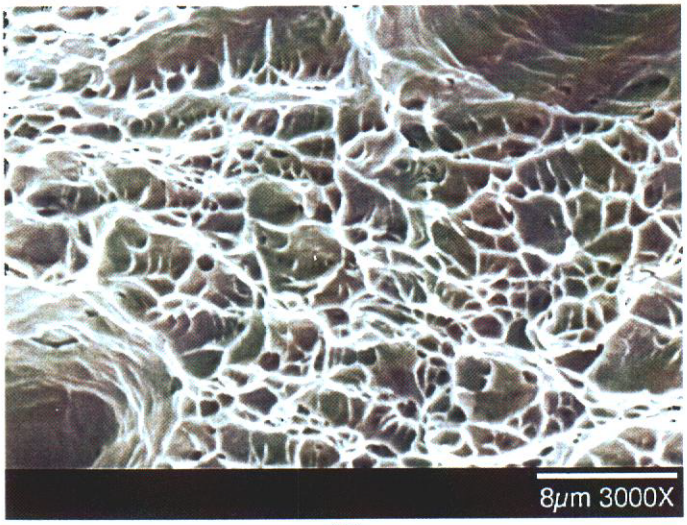

(b)

Figure 5.3. SEM micrographs of fracture surface of an as-deposited tensile sample from a LENS shell build made at 20 ipm. (a) Low magnification showing porosity. (b) high magnification showing ductile microvoid coalescence.

Summary

A limited evaluation of an alloy with significantly slower precipitation kinetics and a transformation response different than H13 tool steel was conducted to identify the effect of these materials characteristics on LENS processing response. In contrast to the H13 results, it was found that 17-4 PH could be deposited in the solution treated condition over a range of processing conditions. Direct aging trials indicated that the precipitation hardening response was similar to that for wrought 17-4 PH. Meaningful measurement of the tensile behavior of the builds was, unfortunately, precluded by excessive porosity in the deposits.

These observations are very encouraging, and suggest that the LENS process has significant potential for tailoring the properties of fabricated structures. This optimism stems from the fact that for complex alloys like 17-4 PH, the solution treated condition is the starting condition from which a wide range of properties can be developed by thermal treatments. Given the localized and controllable heat source inherent in the LENS process, it can easily be envisioned that, following deposition, thermal treatments can be applied *in-situ* to locally manipulate the hardening mechanisms. Comparison of the 17-4 results with those obtained for H13 tool steel illustrates the need for detailed understanding of the material characteristics in relation to the process attributes, and implies that the materials selection criteria for LENS applications are likely to be different than those for more conventional fabrication processes.

References

1. Aerospace Materials Specification AMS 5604D, "Steel, Corrosion Resistant, Sheet, Strip, and Plate 16.5 Cr-4.0Ni-4.0Cu-0.30Cb, Solution Heat Treated, Precipitation Hardenable", Society of Automotive Engineers, Warrendale, PA, (1995).

Section 6. Microstructure Design of 304L Austenitic Stainless Steel

Background

The 300 series austenitic stainless steels are a widely used class of alloys that are known to be sensitive to slight changes in alloy composition, solidification and cooling conditions. These alloys are often used for their elevated temperature and corrosion properties, and sometimes for their non-ferromagnetic characteristics. However, in cast or welded materials the properties can be degraded for a number of reasons. These materials often exhibit a two-phase structure of austenite with several percent ferrite (2-10%) and in the absence of ferrite, exhibit a considerable amount of microsegregation. At elevated service temperature, the ferrite can transform to sigma phase greatly reducing toughness. Ferrite can also affect corrosion behavior and its magnetic characteristics can limit the use of cast material in certain applications. Extensive work has been conducted on welding of the 300 series stainless steels which has shown that alloy composition can have a large effect on solidification mode and microstructure [1-9]. Unique single-phase microstructures have also been observed in high energy density (HED) electron beam and laser welds [2,4-6]. However LENS studies on the 300 series alloys have shown that as is typical for weld structures there materials contained an austenitic matrix with several percent delta ferrite [10].

The goal of this work was to determine if, through computational alloy design, novel microstructures of 304L stainless steel consisting of single-phase austenite with minimal microsegregation could be achieved with the thermal conditions of the LENS process. It was found that ferrite-free and near ferrite-free microstructures were achieved through two different paths. One microstructure was obtained directly through austenite solidification producing a ferrite free microstructure with a small degree of microsegregation. The other microstructure was obtained through ferrite solidification and almost complete transformation to austenite with no detectable degree of microsegregation. The design approach used to obtain such structures and experimental results is discussed below.

Alloy Design

Thermodynamic programs were used both to predict the alloy phase diagram and to provide input into models for predicting solidification behavior and microstructures [11-14]. Using these concepts, several alloys were designed with different Cr_{eq}/Ni_{eq} ratios [15] within the composition range of the Sandia 304L stainless steel specification. The heat compositions and Cr_{eq}/Ni_{eq} ratios of three alloys are given in Table 6.1. The compositions were designed to produce single-phase austenite structures via two different solidification/transformation mechanisms when subjected to the high solidification velocity and cooling rate (estimated at ~10,000°C/s) of pulsed laser welding.

Figure 6-1 shows schematically where the alloy compositions in Table 6.1 may lie on a Ni-Cr pseudobinary diagram. The initial solidification behavior shown in the diagram was

calculated for the average Fe, Mn, Si and C content of the three alloys and different Ni and Cr contents using the thermodynamically based MT Data Program™.

Table 6.1. Heat compositions and Cr_{eq}/Ni_{eq} ratios

Alloy#	Cr	Ni	Mn	Si	C	Cr_{eq}/Ni_{eq}
A	19.7	11.9	1.74	0.59	0.04	1.54
B	20.3	10.5	1.74	0.54	0.03	1.80
C	18.9	9.2	1	.35	.03	1.91

Hammer and Svennson equivalents: Bal Fe

$Cr_{eq} = Cr + 1.37Mo + 1.5Si + 2Nb + 3Ti$

$Ni_{eq} = Ni + 0.31Mn + 22C + 14.2N + Cu$

With conventional welding and casting processes, the critical Cr_{eq}/Ni_{eq} ratio resulting in a change in solidification from primary austenite to primary ferrite is ~1.5 [16-18]. In the absence of any undercooling this composition would correspond to the intersection of the ferrite and austenite liquidus in the diagram in figure 6.1. Thus alloy A with a Cr_{eq}/Ni_{eq} ratio of 1.54 would be expected to solidify as primary ferrite with the secondary solidification of austenite. During cooling most of the solidified ferrite transforms to austenite leaving a two phase ferrite + austenite microstructure. Alloy B with a Cr_{eq}/Ni_{eq} ratios of 1.80 would also solidify as primary ferrite but with less secondary solidification of austenite due to the higher Cr_{eq}/Ni_{eq} ratio. After cooling through the $\delta + \gamma$ field the microstructure would contain some retained ferrite enriched in Cr and depleted in Ni compared to the austenite matrix. Alloy C has the highest Cr_{eq}/Ni_{eq} ratio, 1.91 and may solidify almost completely as ferrite leaving the highest ferrite content after cooling of the three alloys [19,20].

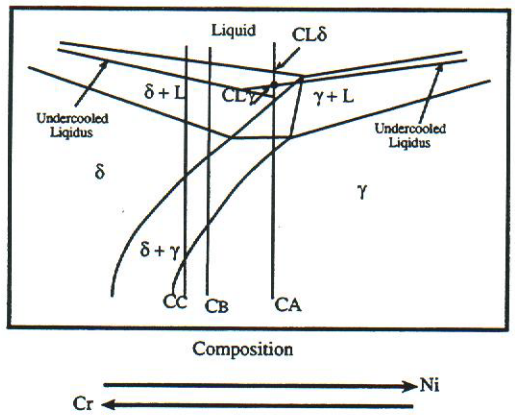

Figure 6.1 Schematic of Fe- Ni-Cr pseudobinary showing approximately locations of the three alloys in Table 6.1.

Under high solidification velocities and cooling rates, different microstructures than those described above may be expected [1,2,4-6,21]. Undercooled d and g liquidus which are dependent upon dendrite tip velocity and to a lesser extent on cooling rate [12,13], are also

drawn in the schematic in figure 6.1. With this degree of undercooling, heat A would solidify as austenite, rather than ferrite, with little or no secondary solidification of eutectic ferrite. The solidified austenite is the equilibrium phase at room temperature. However, with the same undercooling conditions shown in figure 6.1 the undercooled ferrite liquidus of compositions B and C is still above that of austenite. Thus solidification would still occur as primary ferrite but with a larger fraction of ferrite. With sufficient undercooling solidification may occur completely as ferrite. Under rapid cooling rates, the diffusion controlled transformation of ferrite to austenite may be also be suppressed [1,5-9]. As can be seen from figure 6.1 the ferrite may then massively transform to a single phase austenite structure, but unlike alloy A, the austenite is now the product of a solid state transformation. It can be seen that for at the higher Cr_{eq}/Ni_{eq} ratio the ferrite to austenite transformation starts at a lower temperature so the possibly of obtaining a massively transformed structure may be greater.

Experimental Results

LENS builds were fabricated in both the shell and block configurations shown in figure 1.1 Pulsed laser welds made on the deposits verified, as predicted, that single-phase austenite microstructures were obtained. As expected, these welds in alloy A deposits solidified as primary austenite while those in alloys B and C solidified as ferrite and transformed completely to austenite during cooling. It can be seen in figure 6.2 that although both structures are austenite the microstructure is quite different. The primary austenite weld structure in figure 6.2(a) exhibits a relatively large grain size and evidence of microsegregation in the solidification structure. The austenite microstructure of the primary-ferrite solidified laser weld in figure 6.2(b) exhibits a much finer, duplexed, and somewhat faceted grain structure with little evidence of solidification.

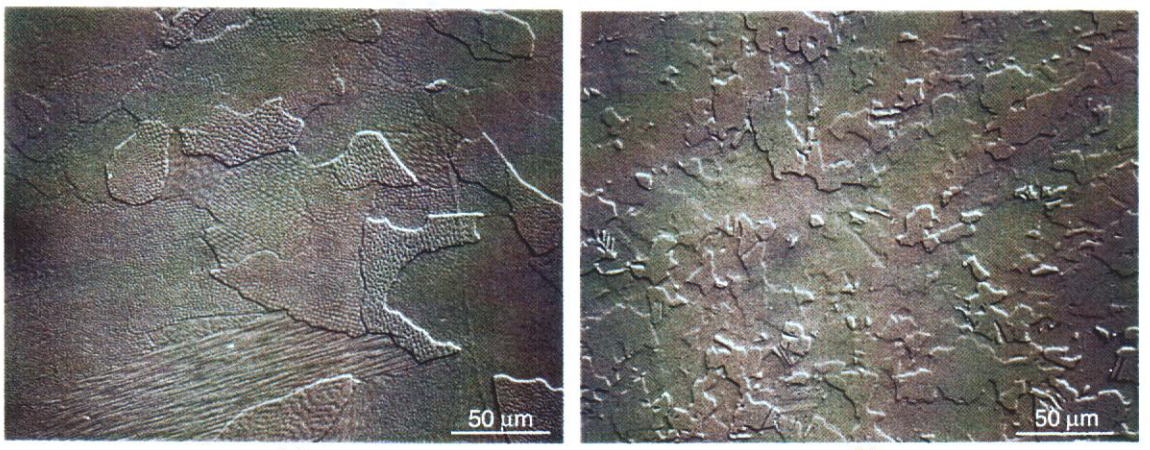

(a) (b)

Figure 6.2. Microstructures of pulsed YAG laser welds in LENS builds: (a) in powder A showing primary austenite solidified microstructure (b) in powder B showing primary ferrite solidified fine grained austenite microstructure.

Both shell and block configurations of alloy A deposited over a wide range in processing parameters exhibited, unlike the laser welds, a two-phase structure of ferrite and austenite. This microstructure, shown in figure 6.3, is typical of those that solidify as primary ferrite with the secondary solidification of austenite. During cooling ferrite is retained along the original dendrite cores. This two-phase microstructure is typical of that reported by other investigators in 300 series stainless steel LENS deposits. We predicted that sufficient undercooling would have occurred at the highest deposition rates of 3.4 cm/sec (80 imp) for solidification to occur as austenite but these calculations were based on a ternary system considering undercooling effects only of Cr. Evidentially for this composition unlike with the laser welds, undercooling was not sufficient to result in austenite solidification.

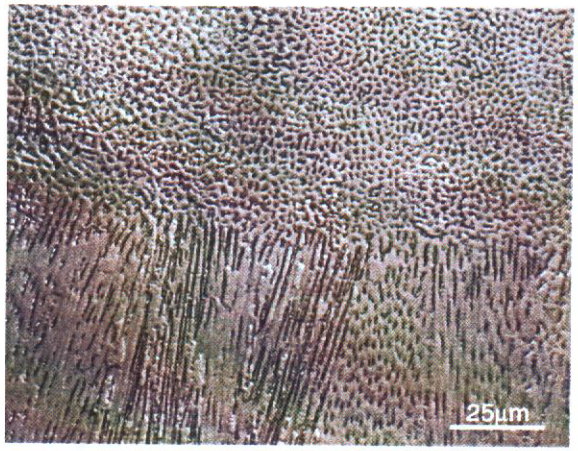

Figure 6.3 Two-phase structure of ferrite and austenite of primary ferrite solidified Block build made form powder of alloy A. Ferrite is in cores of dendrites.

Extensive TEM and STEM analysis was conducted on the two-phase microstructure of alloy A and reported in the literature [22-24]. In most all cases, it was found that the ferrite and austenite exhibited the K-S [25] or N-W [26,27] crystallographic orientations. It was not clear if solidification occurred as a peritectic of ferrite and austenite or as single phase ferrite. The relationship between crystallographic orientation and solidification mode is complex and discussed elsewhere [1,22-24,28-33]. Although there were some ferrite-free dendrite cores the majority of the core regions contained ferrite. The variation in composition between the dendrite cores and boundaries in the ferrite free regions was ~ 4 wt% Ni and ~2 wt% Cr with the dendrite boundaries enriched in Ni and the dendrite cores enriched in Cr.

To promote austenite solidification and a single phase austenite microstructure, several percent Ni power was added to the powder stream using a second powder feeder. The results obtained using this technique are depicted in the microstructure of a shell build shown in figure 6.4(a). The outer surface and the upper portion of the shell build exhibits a two-phase microstructure similar to that of the builds with no Ni addition. However the center of the build exhibits the desired single-phase austenite structure. It was concluded that the two-phase outer case region was due to incomplete mixing in the liquid of the two powder types. These regions correspond to the sides and trailing edge of the melt pool where minimal mixing of the injected powder can occur before solidification. With a dilution of ~2% Ni

only ~ one in fifty powder particles would be Ni. The single-phase region in the center of the build experiences several remelts during subsequent passes resulting in a more uniform structure.

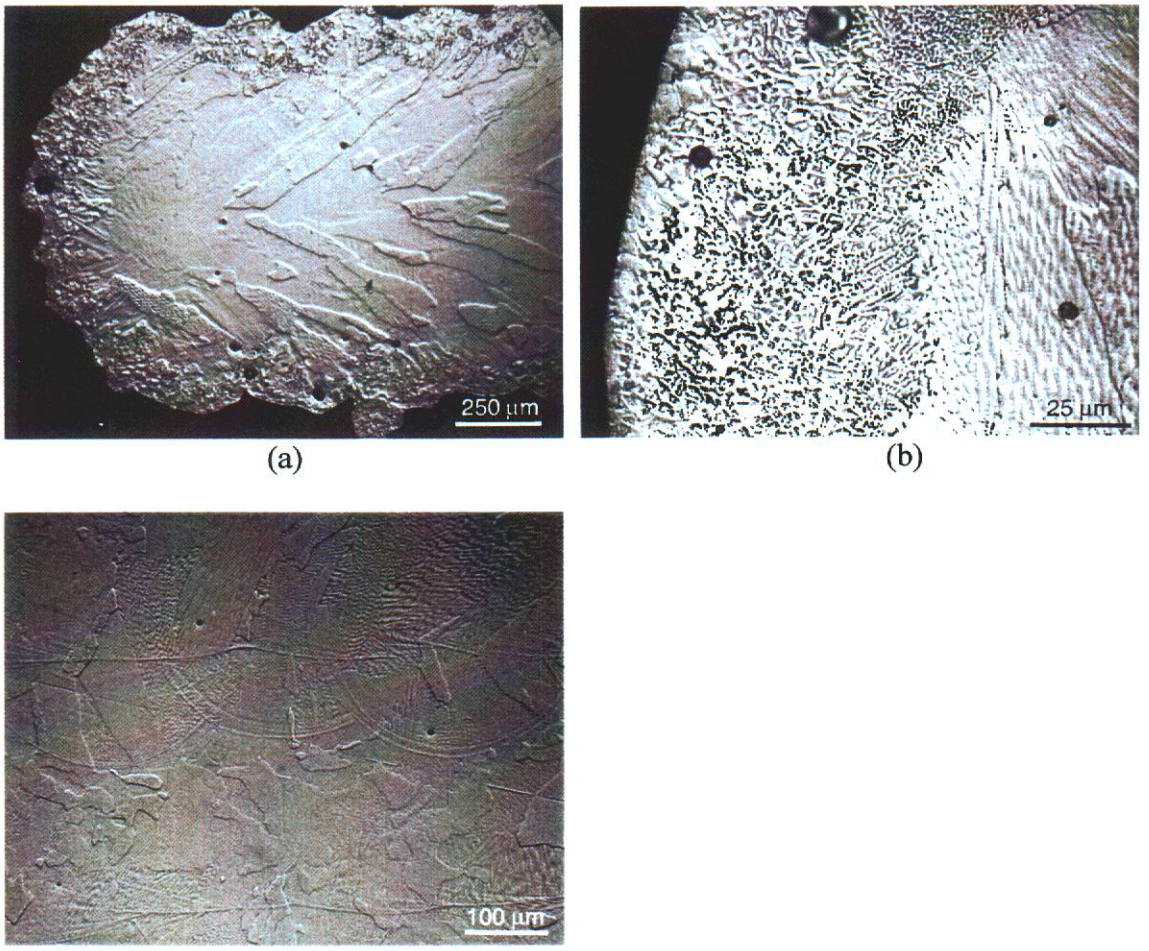

Figure 6.4. Cross sections of build of powder A with a several percent Ni powder addition (a) upper portion of shell build showing a two phase primary ferrite structure at the outer surface and single phase primary austenite center region (b) higher magnification of (a), (c) single phase primary austenite solidified block build showing evidence of different layer and passes.

In low power block builds made from the two powder mixture, Alloy A and Ni, remnants of the two phase microstructure also existed. These regions were confined to the top and sides of the individual passes throughout the build, and were also attributed to lack of mixing. In this case, lack of fusion and interpass porosity also existed. However, under higher power conditions with more remelting, the single-phase microstructure was achieved except again for a thin region at the block surface. The microstructure of the fully dense single phase primary austenite block build is shown in figure 6.4(c). The evidence of the solidification structure is again due to some residual microsegregation.

To determine the degree of segregation of the single phase austenite-solidified structures STEM analysis was conducted across solidification cells. A stem image showing the cellular solidification structure of a shell build is shown in figure 6.5(a). The thickness contrast outlining the cell boundaries results largely from local composition affecting the polishing rate during foil preparation. A STEM analysis was taken in the region shown in the insert of figure 6.5(a). In figure 6.5(b) and (c) it can be seen that microsegregation does exist with the cell boundaries enriched in both Ni and Cr by 3 and 4 wt% respectively. Although the degree of segregation is similar to that measured in the ferrite free regions of the primary ferrite structure of the unalloyed builds, Cr is now enriched at the cell boundaries rather than the cores.

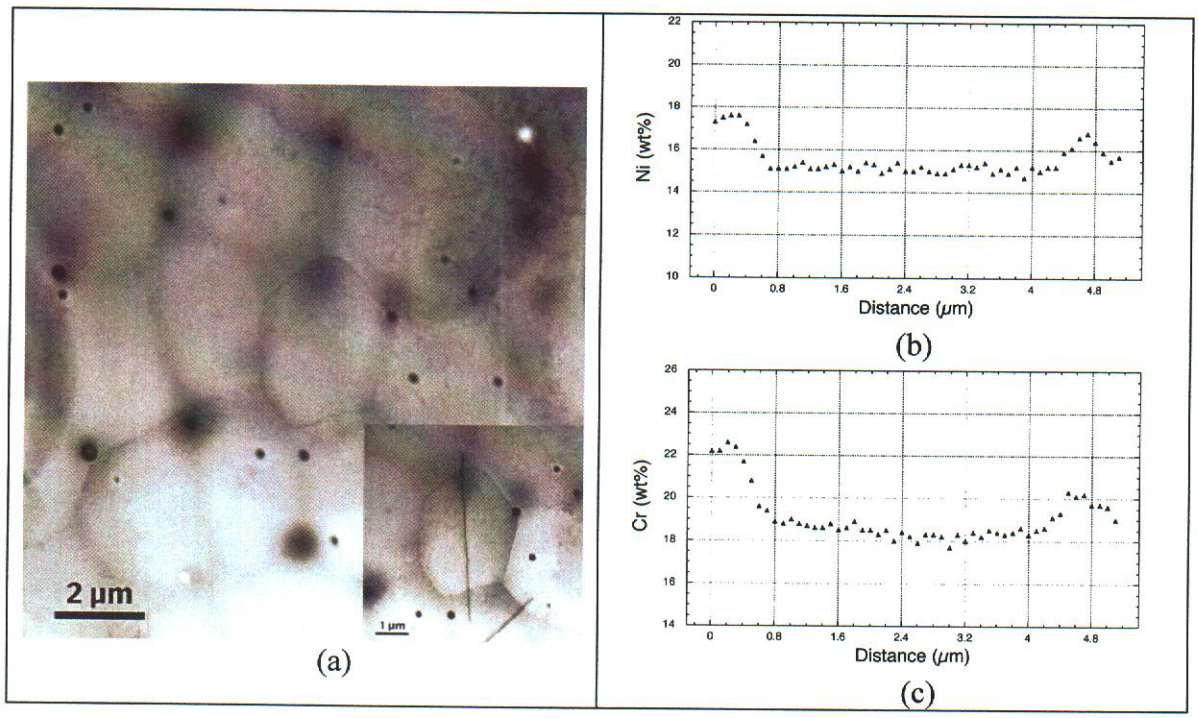

Figure 6.5 (a) STEM Image of primary austenite solidification structure in shell build of powder A alloyed with several % pure Ni showing region of analysis. Results for (b) Ni and (c) Cr

LENS builds of Alloys B and C

The other path to forming a single phase austenite is to solidify as single phase ferrite and massively transform to single phase austenite as was the case for the laser welds on LENS builds of powders lots B and C. A massive transformation occurs by the migration of a disordered interface and involves trans-interphase, interface diffusion but no long range diffusion [34]. Attempts to obtain the single-phase microstructure were unsuccessful when using shell configurations. The typical microstructure of the shell builds with powder B for all processing conditions including processing speeds as high as 3.39 cm/sec are shown in figure 6.6. It can be seen that although the microstructures exhibit some rather large single-phase regions, much of the structure exhibits a lathy or acicular ferrite structure. Note in the

ferrite-free regions, unlike in the austenite structure shown in figure 6.4, no evidence of microsegregation exists. It appears that the entire deposit solidified as ferrite but the cooling rates were insufficient to completely suppress the diffusion controlled transformation of ferrite to austenite.

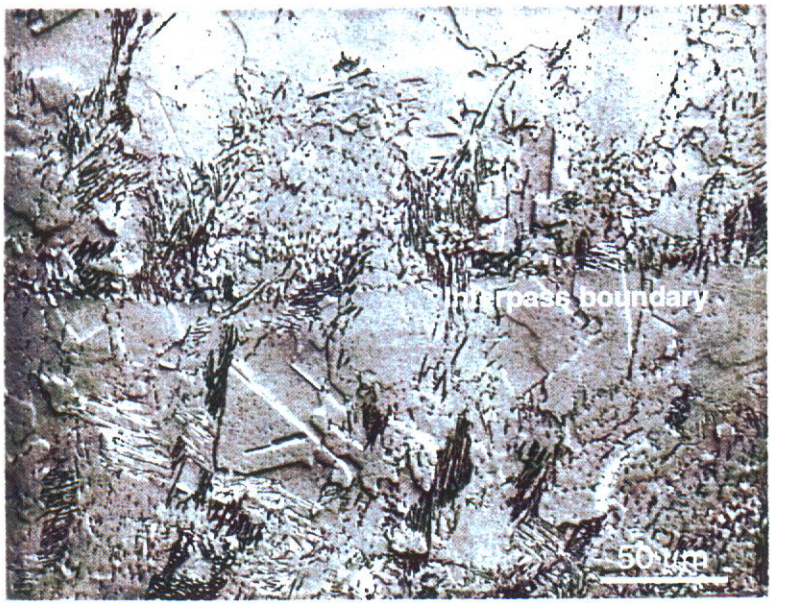

Figure 6.6. Microstructure typical of the shell builds with powder B.

Attempts to develop a single phase austenite were much more successful when using block builds in which the cooling rates are estimated to be at least twice as fast as with the shell builds. The low magnification optical microstructure of a block build of alloy B in figures 6.7(a) exhibits a fine somewhat duplex grain structure. Figure 6.7(b) shows at higher magnification the fine twinned duplex grain structure in the intrapass regions typical of the majority of the sample. The small dark second phase particles are residual ferrite. At the top of the micrograph, ferrite is visible along the HAZ of the upper layer in which the passes run normal to the plane of sectioning. It appears that these regions transform to, or partially to, ferrite on-heating, and do not fully transform back to austenite during cooling.

A distinctively different microstructure existed in the upper region of the top layer of the block builds of powder B as shown at high magnification in figure 6.7(c). This structure existed for ~1/3 the melt depth and is charcteristic of primary ferrite solidification with retained ferrite along the dendrite cores. Strong evidence of microsegregation also exists at the cell boundaries due to the secondary solidification of austenite. Some of the core regions near the center of the micrograph contain a large fraction of ferrite. It is interesting that only the upper portion of the pass exhibits this structure. In the lower region of the pass, where the microstructure more closely resembled that in figure 6.7(b), solidification and cooling rates may have been sufficiently rapid for the material to solidify as single-phase ferrite and transform almost completely to austenite. In block builds of powder B some of the residual solidification structure, although somewhat modified by subsequent high temperature thermal cycles, also existed in other isolated regions of the build. The V-shaped HAZ region of two

overlapping passes containing some of the residual solidification structure is shown at higher magnification in figure 6.7(d). These regions extend furthest into the upper portion of the prior layer. However, in general, the microstructure was somewhat mixed in that there were other isolated regions of the retained solidification structure. This can be attributed to irregularities in the build process as well as variations in local solidification conditions.

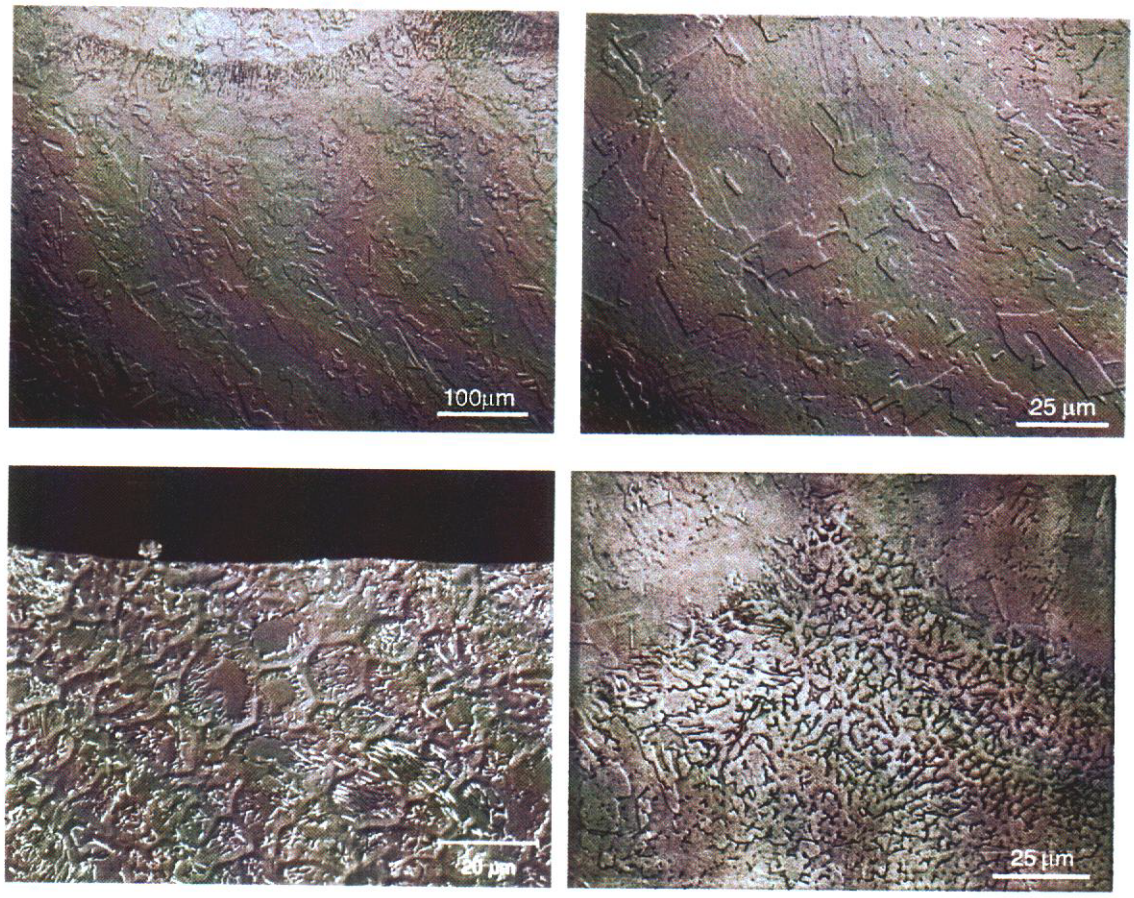

Figure 6.7 Microstructures of block builds of alloy B (a) low magnification showing fine duplex grain structure and ferrite in HAZ of upper layer at top of micrograph (b) higher magnification showing microstructure typical of the majority of the build, (c) upper region of last deposited layer of build showing F/A solidification structure, arrow notes retained ferrite of dendrite cores.(d) retained solidification structure modified by multiple thermal cycles, similar to that in upper right of (a).

The microstructures of block builds of alloy C were similar to those of alloy B except that they contained considerably less ferrite and no residual solidification structure. The microstructure shown in figure 6.8(a) is typical of that of the majority of the build and consists of a fine grain nearly single-phase austenite. However, similar to blocks of powder B, some retained ferrite existed. One region with the highest content of ferrite is shown in figure 6.8(b). This region is in at the intersection of HAZ's of two passes. Similar HAZ structure was observed in the same regions of block builds of powder B, except those builds

contained slightly more ferrite. The upper region of the last pass of builds of powder C exhibited only small amounts of ferrite and solidification structure as shown in figure 6.8(c). However, as noted by the arrow in the micrograph, many of these regions appeared to be associated with a individual spherical power particle.

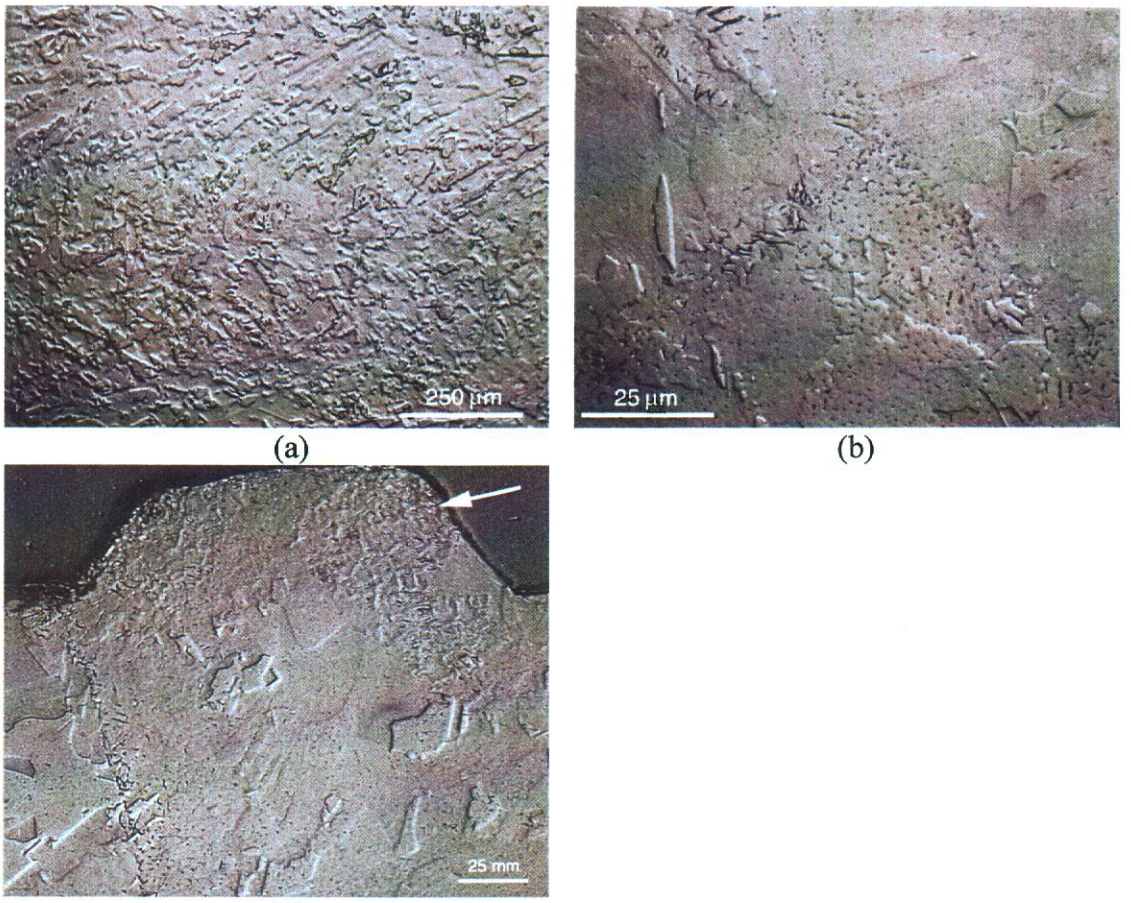

(a) (b)

(c)

Figure 6. 8. Microstructures of block build of powder C: (a) fine grain, nearly single phase austenite structure (b) common HAZ region of two overlapping passes showing retained ferrite (c) top or last layer of build showing solidification structure associated with an individual power particle, and to the left small region of ferrite at interpass boundary.

It should be pointed out that in the block builds about half the previous layer is remelted during deposition of the following layer. Thus the two-phase solidified structure observed in the top pass would be completely re-melted if another layer were deposited. However in powder B in which the solidification structure was extensive, the probability of retained solidification structure is much more likely. The larger region of ferrite/ austenite solidification in powder B, than C, is consistent with its lower Cr_{eq}/Ni_{eq} ratio.
The lower half of the pass which is not re-melted experiences numerous thermal cycles from adjacent passes within the same layer, as well as from those in the next deposited layer. Thus, the final microstructure evolves as a result of solidification and subsequent multiple thermal cycles into single-phase ferrite, two-phase ferrite + austenite, and single phase austenite regions.

The microstructure of the block builds of alloy B was studied using TEM. Very little ferrite was observed in the structure except for the HAZ regions described above. However, it was observed that some of the austenite grain boundaries contained thin regions of ferrite as shown in the TEM micrograph in figure 6.9(a). The ferrite in these regions, in addition to ferrite particles occasionally observed in intergranular regions, figure 6.9(b), exhibited a composition much different than that of the austenite.

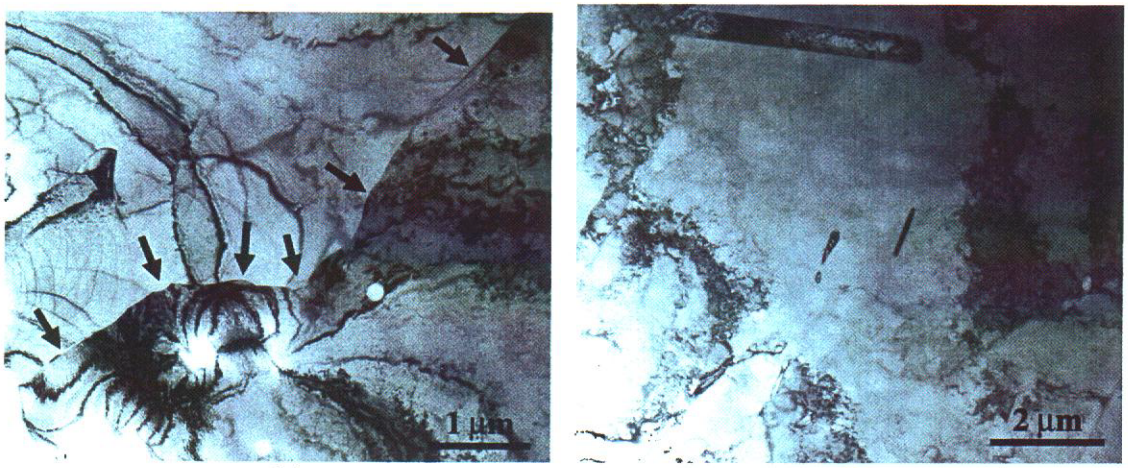

(a) (b)

Figure 6.9. TEM microstructure of block builds of powder B showing (a) thin films of ferrite along regions of the austenite grain boundaries, (b) islands of intragranular ferrite

The grain boundary ferrite may have been enriched in Cr and depleted in Ni as a result of a local diffusional transformation to grain boundary austenite during the cooling process. This ferrite would then not massively transform, see figure 6.1. Likewise incomplete homogenization during solidification and cooling could also lead to localized regions of ferrite as cell cores. The larger single-phase ferrite region of Alloy C than B would allows for more high temperature homogenization of ferrite (In alloy B isolated regions of F/A solidification may also exist.) The onset of the transformation of ferrite to austenite occurs at a higher temperature in composition B than in C that could account for more ferrite in builds of powder B than C. However, transformation behavior is further complicated, in that the onset of the massive transformation can occur at higher temperatures in B than C. (The transformation behavior is discussed in more detail in references 9 and 23.)

The on-heating and on-cooling transformations in the HAZ is complicated by the multiple thermal cycles resulting in non-equilibrium structures. The possibility exists for a massive transformation on-heating as well as on-cooling. The isolated regions of ferrite, figure 6.9, may have formed by a diffusion controlled transformation during heating into the lower temperature two-phase ferrite + austenite region and not completely re-transformed to austenite during cooling. It would be expected that ferrite would form first in the grain boundaries and isolated inhomogeneous regions. Also as noted above, considerably more HAZ ferrite was observed in builds of alloy B than C. This again is likely due to the differences in the high temperature phase equilibria resulting from the different Cr_{eq}/Ni_{eq} ratios. Higher Cr_{eq}/Ni_{eq} ratios than those of alloy C as depicted in figure 6.1 may further

reduce the residual ferrite of the block builds; however, at too high a ratio, the ferrite may be completely retained [2].

STEM analysis was also conducted across the large single-phase austenite regions of block builds of alloy B to compare the extent of microsegregation with that of the primary austenite solidified structures. A STEM image of one of these regions is shown in figure 6.10(a). Since no visual evidence of segregation existed in the STEM images traces were run at 90 degree angles to insure that they would transverse any solidification cellular dendritic structure. Typical analysis for Ni and Cr are contained in figure 6.10(b) and (c). It can be seen that the composition is very uniform in both elements with no measurable degree of microsegregation that was the original goal of the alloy design.

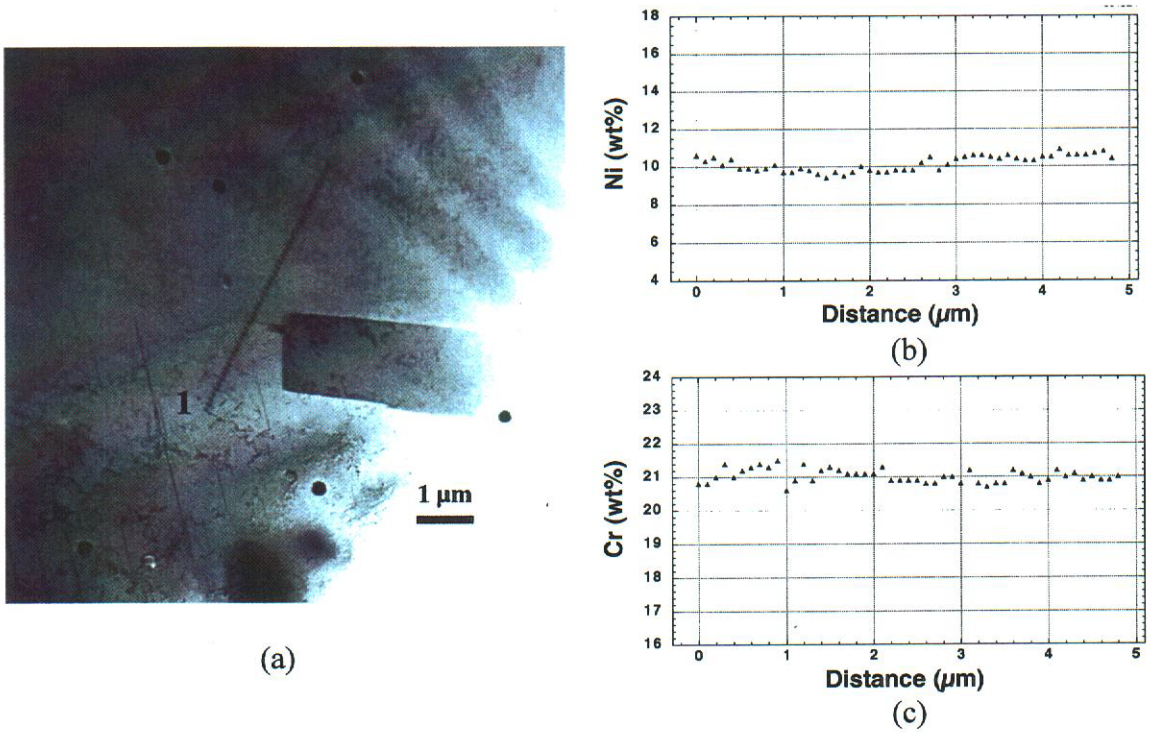

Figure 6.10. STEM analysis of block build of powder B (a) STEM image showing region of analysis, (b) Cr (c) Ni results.

Tensile Properties

The tensile strength of annealed 304L can vary significantly with grains size and dislocation substructure, but typical values are ~30-35 ksi 0.2% YS and ~80 ksi UTS. To compare LENS material properties to those of wrought 304L, tensile specimens were obtained from builds made with the three different powders in addition to alloy A with the Ni modification 304L. It was found that processing conditions had very little if any measurable affect on

tensile properties for a given powder composition and build configuration. Thus for better statistical data, properties shown in Table 6.2 are averages obtained from samples made with different processing conditions. The properties of the shell builds were obtained for both the horizontal and vertical orientations, which showed little directional effects, while only the horizontal orientation was measured in the block builds.

Table 6.2 Tensile Properties

ALLOY	BUILD	YS (ksi)	UTS (ksi)	Uniform Strain (%)	RA%
A	SHELL	50.6	89.2	46	≈ 50
A	BLOCK	57.4	90.2	36	48
A+Ni	SHELL	42.0	75.2	46	48
A+Ni	BLOCK	50.9	72.6	39	59
B	SHELL	50.8	93.8	47	≈ 50
B	BLOCK	56.9	97.3	49	53
C	SHELL	44.7	94.5	48	48
C	BLOCK	53.4	98.8	48.	62

It can be seen that the measured yield strengths of all the LENS deposits exceed 40 ksi. In general the yield strengths of the block builds were 15-20% higher than the companion shell builds due likely to more warm working occurring in the multiple pass block builds. It can also be seen that the single-phase primary austenite solidified structure of alloy A with the Ni additions exhibited by far the lowest UTS of all the samples tested. This is likely due to the fairly large austenite grain size. The fine-grained nearly single-phase austenite structure of alloys B and C exhibited the highest tensile strengths, while all specimens exhibited excellent ductility. Although the single-phase austenite structures obtained with the Ni addition exhibited no ferrite, from a reduced microsegregation and strength standpoint, a single-phase austenite structure that has completely transformed from ferrite provides a far superior structure.

Summary

The concept of using alloying design, based on thermodynamic calculations and solidification models, in conjunction with the high cooling rates of the LENS process was demonstrated using 304L stainless steel. For the alloys selected, it appeared that the rather high cooling rates rather than the more limited solidification velocities could be most effectively utilized to obtain the desired single phase microstructures. In alloy A, dendrite tip

velocities (of ~ 3 mm/s) were insufficient to achieve the desired degree of undercooling to promote primary austenite solidification as they were in the rapidly solidified pulsed laser welds (~1m/sec). However, prediction of tip undercooling are limited with commercial alloys with many alloying additions [13]. Nonetheless, single phase austenite structures were achieved by decreasing the Cr_{eq}/Ni_{eq} ratio through Ni powder additions. Although single phase, this structure did exhibit a small amount of microsegregation.

Nearly single-phase austenite structures were obtained with the block builds of alloys B and C via primary ferrite solidification and complete transformation of the ferrite to austenite. The composition of alloy C with the highest Cr_{eq}/Ni_{eq} ratio and the larger single-phase ferrite region, see figure 1, produced an almost ferrite free microstructure. It is proposed that in this case, the structure solidified as ferrite, homogenized during solidification and cooling and massively transformed to austenite at a sufficiently low temperature where the diffusion controlled transformation could be suppressed.. The structure was completely free of any measurable degree of microsegregation. Still this structure contained a small amount of ferrite, some of which likely formed on heating during subsequent thermal cycles, and did not completely retransform during cooling. This was especially true in the interpass HAZ regions. Higher Cr_{eq}/Ni_{eq} ratios may even further reduce the small amount of ferrite, but at sufficiently higher ratios, the ferrite phase may be nearly completely retained.

Finally, although the tensile yield strengths of the LENS build of both microstructures were considerably higher than those of annealed 304L, the ultimate strengths of the primary ferrite structure were superior.

References

1. J. A. Brooks and A. W. Thompson, International Materials Reviews **36 (1)**, 16 (1991).
2 S. A. David and J. M. Vitek, in *Lasers in Metallurgy*, edited by K. Mukherjee and J. Mazumder (TMS-AIME, Warrendale, PA, 1981), p. 247.
3. J. M. Vitek, A. Dasgupta, and S. A. David, Metall. Trans. A **14A**, 1833 (1983).
4. S. Katayama and A. Matsunawa, in *Proc. ICALEO*, San Francisco, pp.19-25 (1985).
5. J. A. Brooks, M. I. Baskes and F. A. Greulich, Metall. Trans. A **22A**, 915 (1991).
6. J. W. Elmer, S. M. Allen and T. W. Eagar, Metall. Trans. A **20A**, 2117 (1989).
7. S. A. David, J. M. Vitek and T. L. Hubble, Weld. J. **66 (10)**, 289-s (1987).
8. Y. Nakao, K. Nishimoto, and W. Zhang, Trans. JWJ **I19**, 101 (1988).
9. H. Inoue, T. Koseki, S. Ohkita, and T. Tanake,*ISIJ* 1995, 1248.
10. B. P. Somerday, J. A. Philliber, J. E.Smugeresky, "Hydrogen effects on Fracture Direct – Fabricated 304L Stainless Steel", in press SAND report 2001.
11. MT Data software licensed to AEA Technologies
12. W. Kurz and D. J. Fisher, *Fundamentals of Solidification,* (Trans Tech Publications Ltd., Switzerland, 1989).
13. S. Fukumoto and W. Kurz, ISIJ International **37 (7)**, 677 (1997).
14. J. W. Elmer, in *The Metals Science of Joining*, edited by M. J. Cieslak, Perepezko, Kang and Glicksman, (TMS, Warrendale, PA, 1992) pp.123-133.
15. O. Hammer and U. Svensson, in *Solidification and Casting of Metals* (The Metals Society, London, 1979), p. 401.
16. T. Takalo, N. Suutula and T. Moisio, Metall. Trans. A **10 (4)**, 1173 (1979).

17. N. Suutula, Effect of solidification conditions on the solidification mode in austenitic stainless steels, *Acta Universitatis Ouluensis, Series C Technica* **23**, (University of Oulu, Oulu, Finland 1982).
18. N. Suutula, T. Takalo and T. Moisio, Metall. Trans. A **10 (4)**, 512 (1979).
19. C. J. Long and W. T. DeLong, Weld. J. **52**, 281-s (1973).
20. WRC 92 diag
16. B. Laursen, F. Olsen, J. Yardy and T. Funder-Kristensen, in *International Conference on Welding and Joining Science and Technology*, Madrid, Spain, (ASM, 1997) pp. 571-580.
17. J. Brooks, T. Headley, and C. Robino, Materials Research Society, Symposium Y Proceedings, April 2000 (in press).
18. T. Headley and J. Brooks, Solidification and Microstructural Evolutions of LENS Deposisted 304L Stainless Steel. Submitted to Metall. Trans. A.
19. J. Brooks, T. Headley and C. Robino and J. Puskar, Microstructure and Properties of LENS Deposited 304L Stainlees Steel. Submitted to Metall. Trans. A.
20. G. Kurdjumov and G. Sachs. *Z.Phys*., 1930,**64**,.325-343.
21. S. Nishiyama, Sci. Rept., Tokyo Univ. **23**, 369 (1993).
22. G. Wasserman, Ach. Eisenhuttenwesen **16**, 647 (1933).
23. J. A. Brooks, N. Yang and J. Krafcik, in *Recent Trends In Welding Science and Technology*, edited by S. A. David and J. M. Vitek, (ASM International, 1992).
24. H. Inoue, T. Koseki and S. Ohkia, Effect of solidification and subsequent transformation on ferrite morphologies in austenitic stainless steel welds, IIW Doc. IX-1835-96.
25. H. Inoue, T. Koseki and S. Ohkia and M. Fuji, Formation mechanism of vermicular and lacy ferrite in austenitic stainless steel weld metal, Nippon Steel Corporation
26. V. Kujanpaa, N. Suutala, T. Takalo, and T. Moisio, Weld. Res. Int., 1979,**9**, (2), 55-76.
27. N. Suutala, T. Takalo, and T. Moisio, Metall Trans., 1980,**11A**, (2), 717-725.
28. N. Suutala, and T. Moisio, "Solidification technology in the foundry and casthouse", 310-314;1983, London, The Metals Society.
29. T. Massalski, in Phase transformations", 433-468; 1970, Metals Park, OH, American Society of Metals.

Section 7. Ceramic-to-Metal Transitions

Introduction

The fabrication of ceramic-to-metal transitions by LENS processing was envisioned as a stretch goal for the program. This conservatism was based in the knowledge that ceramic materials are extremely difficult to process by fusion techniques, Moreover, the localized heating and steep thermal gradients inherent in laser based processes, coupled with the limited ductility of ceramic materials, implies that thermally induced strains and cracking were likely to be problematic. Nevertheless, it was believed that the potential benefits and implications of the ability to directly fabricate monolithic structures containing ceramics and metals was worthy of investigation. A limited investigation of this concept was therefore conducted.

Direct Ceramic Deposition

As a first step of the fabrication of ceramic materials, different grades of aluminum oxide substrates were heated with the laser to determine to what extent melting could be achieved. Melting was successful, but extreme microcracking was observed on all three grades of alumina: diamonite, 80% and 95% alumina (balance SiO_2). The nature of the microcracking is shown in figure 7.1 for the 95% alumima. In spite of the cracking aluminum oxide powder was directly deposited onto an aluminum oxide substrate to determine the nature of melting of the injected powder particles. The laser was again used to create a melt pool in the substrate into which the powder was deposited. Depositing the alumina powder in this manner was partially successful as the powder melted and both lines and multi-pass walls were built. However, the resulting structures were extremely fragile and again exhibited significant microcracking. Furthermore, the resulting structures did not appear to be aluminum oxide, but rather some sort of mixture of aluminum oxide and a glassy phase as evidenced by the green color of the deposits. Processing with some amount of oxygen in the chamber atmosphere would probably be of advantage for this type of deposition.

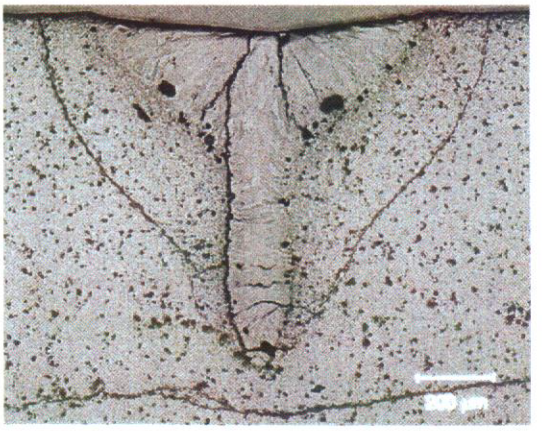

Figure 7.1. Cross section of laser melte aluminum oxide. Note microcracks in tl melted zone, in the region surrounding tl region, and at bottom.

Direct Metal-to-Ceramic Deposition

The next series of evaluations focused on a discrete transition from a ceramic to metal and involved depositing titanium powder onto aluminum oxide substrates. Selection of this material system was based on the known reactivity of titanium relative to aluminum oxide (e.g. as it is applied in reactive brazing alloys). A –100/+325 mesh titanium powder was used as the LENS build material with aluminum oxide substrates that were approximately 50cm x 25cm x 13cm thick. It was possible to deposit a single line of titanium material onto the substrate that resulted in a well bonded interface. However, while it was possible to deposit titanium in a single line, cracking was often encountered in the substrate alumina. It is likely that the cracking was due to the steep (and unavoidable) thermal gradients present between the molten pool of titanium and the ceramic substrate, and could therefore not be eliminated by varying the processing conditions. Attempts to moderately preheat (e.g. to approximately 400°C) the ceramic substrate prior to deposition did not reduce the propensity for cracking.

Since the goal of this project was to fabricate full three-dimensional parts, several attempts were also made to deposit, in spite of the cracking which occurred in the single line deposits, multiple passes of titanium onto the ceramic substrate. In all cases, cracking occurred. The cracking was typically found in the ceramic substrate, but it also occurred in the titanium deposits as well. One of the problems (and advantages) associated with the titanium processing is titanium's affinity for oxygen. Although the reaction between the titanium and the alumina promotes bonding, the uptake of oxygen into the titanium likely results in reduced ductility and the propensity for cracking in the metal.

It therefore appears that direct deposition of structural metallic alloys onto ceramic substrates, though perhaps not impossible, is extremely problematic. Certainly, it seems likely that low meting temperature and/or low strength alloys could indeed be successfully deposited, but it is unclear that there would be any practical advantages to this relative to conventional processing. It also seems probable that extreme preheating, to the order of 1000°C or more, could sufficiently reduce the thermal gradients and hence cracking in the ceramic. Here again, however, it is difficult to envision circumstances where this would result in an advantage relative to more conventional processing such as ceramic-to-metal brazing. Certainly, there may be situations where hybrid processing would be advantageous. For example, brazing of a metal interlayer onto a ceramic substrate, for the purpose of providing a surface onto which a near net shape metallic features could be deposited, may have some utility for the fabrication of complex structures.

Graded Transitions

Since a discrete transition from a ceramic to a metal was not successful for building a full three-dimensional part, a graded transition was investigated. The goal of these experiments was to minimize the thermal mismatches that were generated by processing. Initially,

ceramic powders were premixed with titanium powder in discrete ratios and the premixed powder was deposited. Multiple ceramic powders were mixed including aluminum oxide, boron nitride and silicon carbide. Volume ratios of 5, 10 and 20% of ceramic powder were mixed. Ultimately, the goal was to transition from one material to another through a graded interface by using two powder feeders instead of premixed compositions. This co-depositions of ceramic and metal powders was somewhat successful. The substrates were titanium and typically only one layer was deposited. Given the relative success of mixing ceramic powders into the melt pool, an experiment was planned to deposit onto a robocast cermet substrate. Unfortunately, a suitable robocast substrate could not be obtained before the termination of the project.

Metal Matrix Composites

Parts made from titanium and aluminum have traditionally had difficulties with lubrication and wear. Recently, it has been discovered that if an aluminum or titanium part has a surface that is essentially a metal matrix composite containing ceramic particles and a solid lubricant particles, these parts are essentially self lubricating and exhibit good wear performance. The manufacturing of these parts is currently cost prohibitive, however. Since earlier attempts to deposit metals with ceramic particles showed promise for depositing single layers, it was decided that the addition of a solid lubricant could provide a cost-effective solution. Thus, In addition to mixing ceramic powders with the titanium powders, several attempts were made to also add solid lubricants into the deposits.

Initially, molybdenum disulfide was mixed with titanium powder and ceramic powders of aluminum oxide, boron nitride and silicon carbide. Due to the relatively low melting temperature of the molybdenum disulfide, 1185 ° C, compared with the melting point of titanium, 1800 ° C, the molybdenum disulfide appeared to be dissolved in the titanium matrix. Thus, tungsten disulfide, which has a higher melting temperature than molybdenum disulfide, was therefore evaluated as the solid lubricant additive. Figure 7.2 shows a successful metal matrix composite of tungsten disulfide in titanium deposited by the LENS technique. The tungsten disulfide particles are uniformly distributed throughout the titanium matrix, and appear to be well bonded to the matrix. Figure 7.3 shows a similar LENS deposit consisting of alumina particles dispersed in a titanium matrix. In general, both deposits appear to be essentially fully dense and are likely to exhibit useful properties.

Figure 7.2. Optical micrograph of LENS de
of titanium containing dispersed tungsten d
particles.

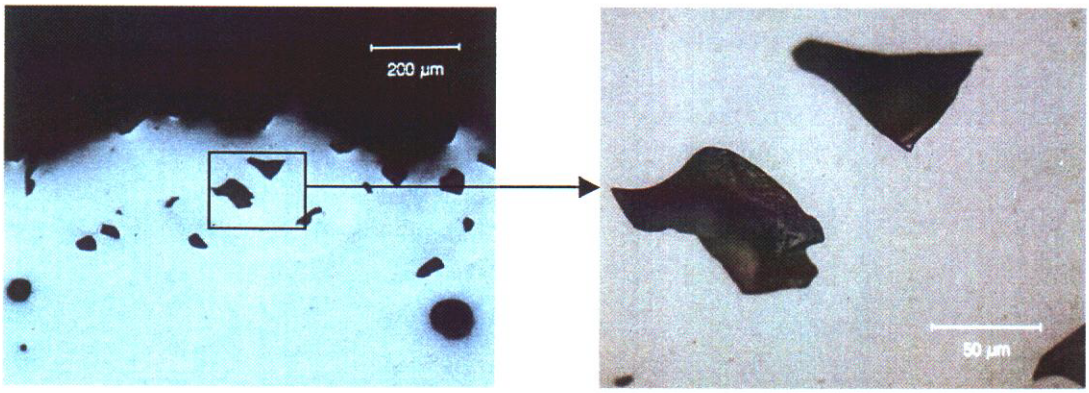

Figure 7.3. Optical micrographs of titanium LENS deposit containing dispersed Al_2O_3 particles. Note the particles retain their angular features and are not cracked.

Summary

Attempts to fabricate ceramic and metal-to-ceramic LENS deposits were generally unsuccessful due to cracking in the ceramic component of the build. It is believed that the cracking is a result of the steep thermal gradients inherent in the LENS process, and could not be avoided by changes in processing parameters. Although it may be possible to overcome some of these difficulties through preheating, advantages relative to other, more conventional, processes remain unclear.

Initial trials directed at incorporating ceramic particles into metallic LENS structures were successful, and indicate that metal matrix composites can potentially be fabricated by the LENS process. Thus, although the direct ceramic-to-metal transitions were somewhat disappointing, the encouraging results obtained for the metal matrix composites imply that the LENS process may be appropriate for the fabrication of these types of novel structures.

Section 8. Porosity in LENS Powders and Deposits

As noted in the previous sections porosity in some cases was found to be a severe problem. It was noted in Section 5 that porosity was so extensive in the 17-4 deposits that meaningful tensile strengths and ductilities could not be measured. It was also noted in Section 6 that porosity in the outer regions of the builds was clearly identified with individual powder particles. Thus it was decided that it was imperative to determine the primary source of defects including lack-of-fusion (LOF) at interlayer boundaries but especially spherical, intralayer porosity. It has been found that LOF defects are minimized by adjusting processing parameters, but the cause(s) of spherical, intralayer porosity are not clearly understood and no method has been available to remove spherical porosity. In this study, porosity was characterized in relation to starting LENS powders. Five lots of powder from different manufacturers, one lot of 17-4PH and four lots of 304L (304L-1,2,3, and 4) were characterized and then used to produce LENS builds. Thin shell and 3-D block (see figure 1.1) builds were deposited with laser power 520 to 700W, powder feed rate 30 to 36 g/min, and travel speed 50 to 200 cm/min. A detailed description of the results of this study are found in Reference [1]. Results of this study show the importance of careful characterization and specification of starting powders on the quality of the final LENS deposits. In particular, for given LENS parameters, powders with the lowest porosity should be specified to minimize LENS deposit porosity.

Pore Morphology and Deposit Microstructure

The 17-4PH powder (figure 8.1a) contained large amounts of porosity from the atomization process. As shown by others [2], voids within powders contain the argon atomizing gas. Sample 304L-4 (figure 8.1b) contained the lowest porosity content of all the lots analyzed. As shown in figure 8.1, both powders and voids were approximately spherical in shape.

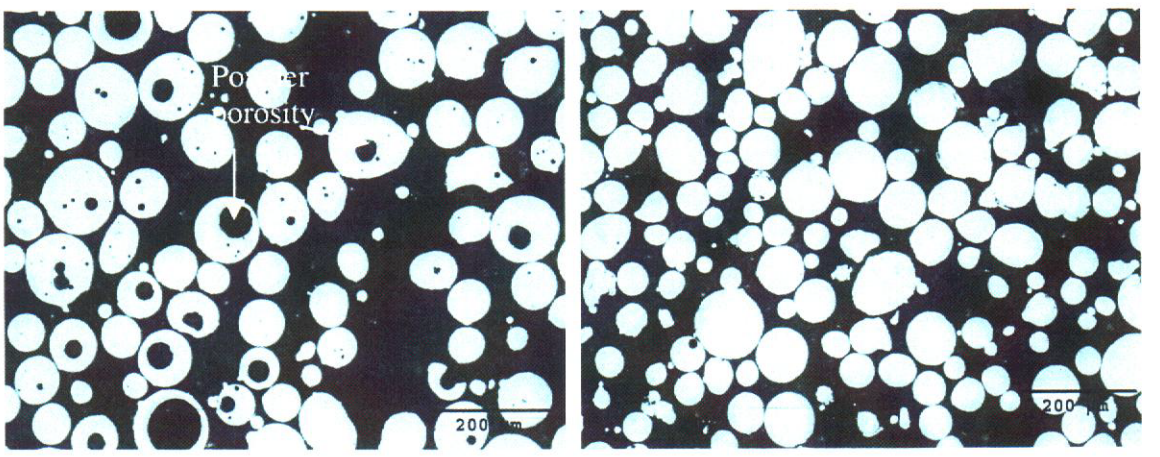

(a) (b)

Figure 8.1. Photomicrographs of as-polished (a) 17-4PH and (b) 304L-4 LENS powders.

In LENS deposits (figure. 8.2), the LOF and spherical porosity can be distinguished. Unmelted or partially melted particles are also found between layers and along the surface of deposits. Small voids were found remaining within the individual particles, strongly suggesting that particle porosity may directly contribute to deposit porosity. The microstructures of stainless steel LENS deposits are also apparent in figure 8.2. The 304L-3 block build (figure 8.2a), contains mostly austenite, which transformed from delta ferrite on cooling. Only a small amount of the original ferrite is retained, not visible at this magnification. The 17-4PH deposit (figure. 8.2b) most likely solidified as delta ferrite, transformed to austenite, and then to martensite on cooling. The block 304L-2 deposit (figure. 8.2c and d) structure is mostly austenite, and contains a different ferrite morphology than 304L-3.

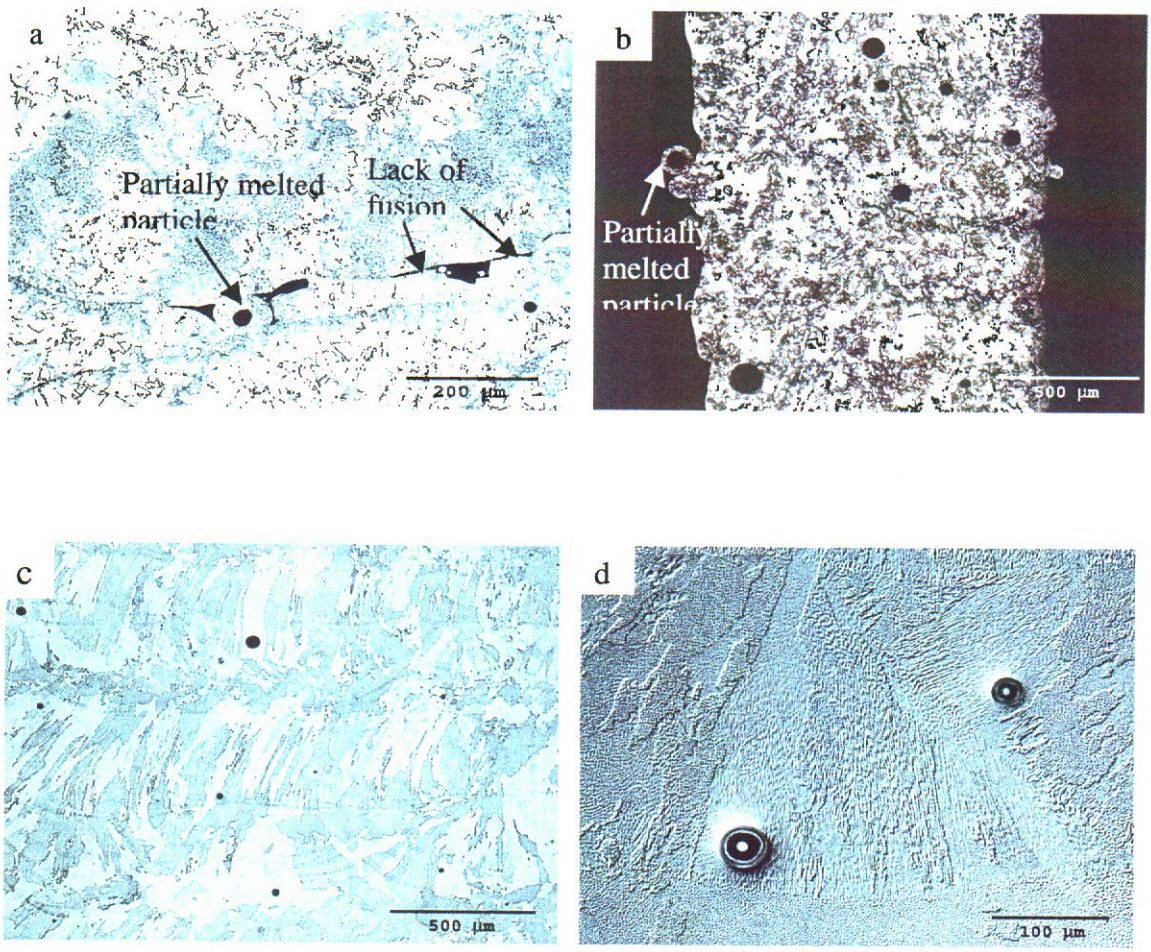

Figure 8.2. (a) Photomicrograph of interlayer lack of fusion in 304L-3, block LENS build. (b) Cross-section of 17-4PH, shell build showing spherical porosity. (c) Low magnification photomicrograph of spherical porosity in 304L-2, block build. Note smaller size and amount of pores in 304L compared to 17-4PH.(d) Higher magnification view of spherical porosity (differential interference contrast).

Porosity Content

Based on image analysis measurements (area %), the spherical porosity content in the deposits is lower than in the starting powders (figures 8.3a and b). A qualitative correlation between the starting powder and the deposits is found for a given lot of material. For example, lot 304L-4 exhibited the lowest porosity in both powder and deposits while 17-4PH had high porosity levels in powder and deposits. However, the effects governing deposit porosity are likely more complex than a one-to-one correlation between powder and deposit, possibly depending on details such as the relative sizes of voids and powder particles.

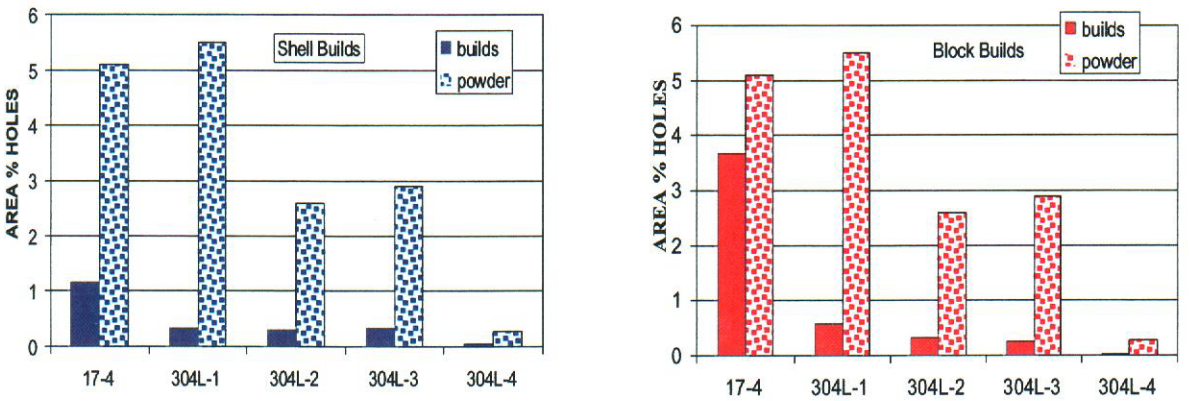

(a) (b)

Figure 8.3. Porosity measurements in powders and LENS builds: (a) shell builds, (b) block builds. Laser travel speed was 100 cm/min for all deposits.

Measured Size Distributions

Powder and pore size distributions were determined and an example is shown in figure 8.4a. The histogram displays the size distribution of pores within powders (see figure 8. 1). When preparing 2-D cross-sections the voids are intersected at various depths, not always at their center, resulting in an error in favor of smaller voids. For spheres, a correction procedure was applied to extract N_V, number per unit volume, from the measured N_A, number per unit area. The relative amounts of voids of a given size are then changed, since many of the smaller voids in the raw data are actually sections of larger ones. The resultant pore size distributions were then curve-fit with a truncated log-normal relationship. For voids within particles, the void sizes must be smaller than the particles in which they are contained. Ratios of average void size (based on spherical geometry) to average particle size are shown in figure 8.4b. Although the use of average values gives only a rough estimate of overall powder characteristics, it is evident that there are differences in the size of the voids relative to particle size in these powder lots. In particular, powder lot 304L-1 contains large voids,

on average, relative to its particle size. The results suggest that the relative size of voids within the particles may be important. For the same starting void content, larger void/particle size ratios tend to result in less porosity (e.g. 304L-1). The effect may be due to a mechanism whereby gas escapes from the melt pool surface, since buoyancy increases significantly with gas pore size.

The size distributions of starting powders and of voids within deposits were characterized in a similar manner and the results are found in Reference [1]. In LENS deposits, the voids are larger than in the starting powders [1]. This may indicate that some pores form by accumulation of gas from several particles. However, no quantitative relation could be made between void size in the powders and resultant deposits, possibly due to other effects such as entrapment of powder-feed gas.

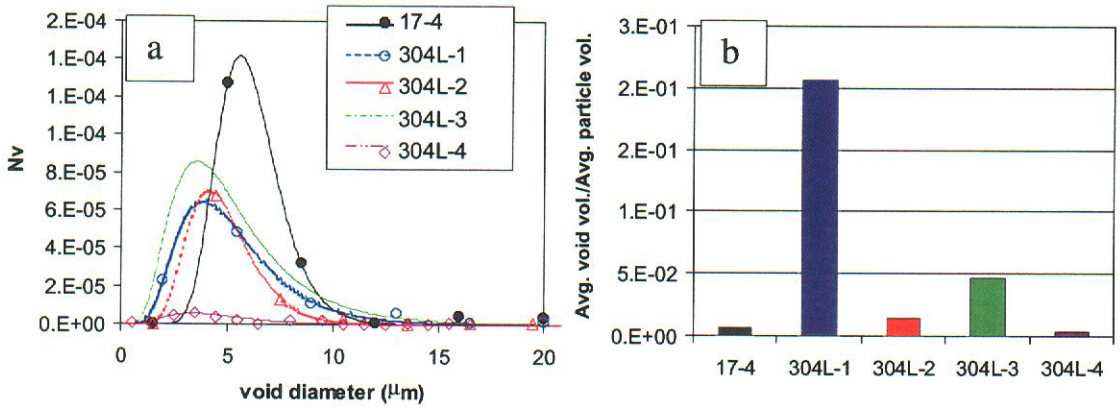

Figure 8.4. (a) Summary histograms of voids within starting LENS powders. (b) Ratio of average void volume to average particle volume for LENS powders.

Effect of Remelting on Void Reduction

If it is assumed that porosity is reduced by gas escape from the liquid melt pool, then remelting should cause a decrease in porosity. To investigate this effect, 17-4PH builds were produced (with high porosity content ~ 5%) and allowed to cool to room temperature. Then the top 1-2 layers were remelted with the laser. No additional powder was injected during the remelt process. Figure 8.5 shows that considerable reduction in porosity is obtained from the remelting process. Although the remelt process appears to be effective, for practical LENS application it is clear that selection of low porosity powder from the start is a more efficient method to avoid porosity. In addition, the remelt process delivers additional heat input to the deposit and may thereby affect the underlying microstructure and properties more than for typical surface layer deposition.

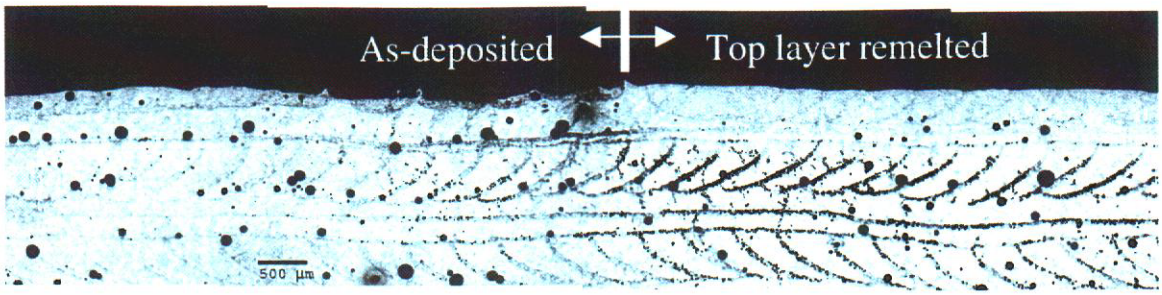

Figure 8.5. Photomicrograph of top layers of 17-4PH LENS deposit (etched condition). On right side of image, the top 1-2 LENS layers have been remelted.

Summary

Atomized powders, voids within powders, and voids within deposits are spherical in shape and generally follow log-normal size distributions. In general, starting LENS powders with high porosity content result in deposits with increased porosity. Differences were observed between 17-4PH and 304L, with 17-4PH showing generally higher porosity content in powders and deposits. The process of laser remelting was shown to decrease LENS porosity content. Although remelting seems effective, for practical LENS application the selection of starting powders with low porosity is a more efficient method to avoid porosity in final LENS deposits.

References

1. D.F. Susan, J.D. Puskar, J.A. Brooks, and C.V. Robino, Porosity in Stainless Steel LENS Powders and Deposits, 11th Solid Freeform Fabrication Symposium, Austin, TX, Aug. 2000.

2. B.H. Rabin, G.R. Smolik, and G.E. Korth, Mat. Sci. and Eng. A, A124, pp. 1-7, 1990.

Section 9. Publications Funded, or Partially Funded, Under LDRD Program

1. M. L. Griffith, M. E. Schlienger, L. D. Harwell, M. S. Oliver, M. D. Baldwin, M. T. Ensz, J. E. Smugeresky, M. Essien, J. Brooks, C. V. Robino, W. H. Hofmeister, M. J. Wert, D. V. Nelson, *Thermal Behavior in the LENS Process*, proceedings of the Solid Freeform Fabrication Symposium, August, 1998, Austin, TX, p. 89.

2. W. Hofmeister, M. Wert, J Smugeresky, J. Philliber, M. Griffith, and M. Ensz *Investigation of Solidification in the Laser Engineered Net Shaping* (LENS^{TM}) *Process*, JOM, Vol. 51, No.7, 1999

3 J. Brooks, C. Robino, T. Headley, S. Goods, M. Griffith, *Microstructure and Property Optimization of LENS Deposited H-13 Tool Steel,* Solid Freeform Fabrication Symposium *1999*, Ed. D. Bourell,J. Beaman, R. Crawford, H. Marcus and J. Barlow, U. of Texas at Austin, (1999) pp. 375-382.

4. J. Beuth, A. Vasinonta, and M. Griffith, *Process Maps for Laser Deposition of Thin-Walled Structures*, proceedings of the Solid Freeform Fabrication Symposium, August, 1999, Austin, TX, p. 383-391

5. M. Griffith, E. Schlinger, L. Harwell, M. Oliver, M. Baldwin, M. Ensz, J. Brooks, C. Robino, J. Smugeresky, W. Hofmeister, M. Wert, and D. Nelson, *Materials and Design*, Vol. 20, Elsevier Science Ltd, (1999), pp. 107-213.

6. M. L. Griffith, M. E. Schlienger, L. D. Harwell, M. T. Ensz, D. L. Greene, J. E. Smugeresky, C. V. Robino, W. H. Hofmeister, M. J. Wert, D. V. Nelson, *Understanding Thermal Behavior in LENS Processing of Structural Materials*, Proceedings of The Mineral, Metals, and Materials Society Conference, March 3, 1999, (in press).

7. M. L. Griffith, M. E. Schlienger, L. D. Harwell, M. S. Oliver, M. D. Baldwin, M. T. Ensz, J. E. Smugeresky, M. Essien, J. Brooks, C. V. Robino, W. H. Hofmeister, M. J. Wert, D. V. Nelson, *Understanding Thermal Behavior in the LENS Process, Journal of Materials Design*, volume 20 number 2/3, June 1999, p 107-114.

8. J. Brooks, T. Headley, and C. Robino, *Microstructures of Laser Deposited 304L Austenitic Stainless Steel,* Materials Research Society, Symposium Y Proceedings, April 2000 (in press).

6. A.Vasinonta, J. L. Beuth, M. L. Griffith, *A Process Map for Consistent Build Conditions in the Solid Freeform Fabrication of Thin-Walled Structures*, accepted to Journal of Manufacturing Science and Engineering, July 2000.

7. D.F. Susan, J. D. Puskar, J. A. Brooks, and C.V. Robino, *Porosity in Stainless Steel LENS Powders and Deposits*, 11th Solid Freeform Fabrication Symposium, Austin, TX, Aug. 2000.

11. A. Vasinonta, J. L. Beuth, M. L. Griffith, *Process Maps for Controlling Residual Stress and Melt Pool Size in Laser-based SFF Processes*, to be published in proceedings of the Solid Freeform Fabrication Symposium, August, 2000, Austin, TX.

12. J. Brooks, T. Headley and C. Robino and J. Puskar, Microstructure and Properties of LENS Deposited 304L Stainless Steel, to be submitted to Metall. Trans. A.

13. T. Headley and J. Brooks, Solidification and Microstructural Evolutions of LENS Deposited 304L Stainless Steel, to be submitted to Metall. Trans. A.

Report Summary

Summaries of the individual components of this LDRD are contained at the end of each section. It was shown that the increased understanding of the LENS process, from thermal behavior to porosity formation, can be applied in a scientific way to increase quality and functionality of LENS fabricated components. For example, the capability developed in this program to measure thermal fields was used to develop and validate thermal models to control residual stresses. Furthermore, it was demonstrated that the unique thermal conditions of the LENS process can, in certain cases, be controlled to optimize build microstructure and properties. This was demonstrated using the secondary hardening tool steel H-13. However, to utilize the high solidification velocity and cooling rates, alloy compositions must be designed to provide the ability to tailor desired microstructure as shown for the case of the austenitic stainless steel 304L. In this case unique microstructures with excellent properties were achieved. However, it was also demonstrated that for some alloy types, aging kinetics are too sluggish to be manipulated through LENS process control. This was demonstrated with the precipitation strengthened martensitic stainless steel 17-4 PH. However, in this case the rather sluggish aging kinetics allows, with a simple post build heat treatment, the ability to achieve properties at least equivalent to those achieved through wrought metallurgical processing. The capability developed in this program to feed multiple powders at controlled rates allows one to design components with different compositions and properties in different regions of the component to meet unique engineering requirements. This is a very attractive attribute when processing to a near net shape configuration. Finally, it was shown that the processing of ceramics and transition from metals to ceramics appears in some cases to be feasible. However, a considerable effort would be required to successfully develop this technology.

During the time of this LDRD it became evident through interactions with design engineers, that the increased understanding and development of the LENS process makes this technology very attractive for a variety of Sandia components. However, to fully achieve the capabilities of this technology will require solid materials support.

Acknowledgements

The authors greatly acknowledgement the assistance of M. Oliver, L. D. Harwell, M. T. Ensz, P. Duran, for LENS processing, A. Newman for experimental support, and A. Gardia, and A. Kilgo for metallographic support.

Distribution

Los Alamos National Laboratories
Attn: Gary Lewis
MS G770 MSR-6
P.O. Box 1663
Los Alamos, NM 87545

Los Alamos National Laboratories
Attn: George T. Gray III
MS G755 MST-8
P.O. Box 1663
Los Alamos, NM 87545

Los Alamos National Laboratories
Attn, J. D. Katz
MS G770 MST-6
P.O. Box 1663
Los Alamos, NM 87545

Los Alamos National Laboratories
Attn, John Milewski
MS G770 MST-6
P.O. Box 1663
Los Alamos, NM 87545

Oak Ridge National Laboratory
Attn: Dr. Stan David
Metals and Ceramics Division
Bethel Valley Road
PO Box 2008
Oak Ridge, TN 37831-6095

Ohio State University
Materials Science and Engineering
Attn: Prof. Hamish Fraser
116 W Nineteenth Ave
141 Fontana Laboratories
Columbus, OH 43210

Lehigh University
Department of Materials Science
Attn: Prof. John DuPont
Whitaker Laboratory
5 East Packer Ave
Bethlehem, PA 18015

Savannah River Site
Attn: Dr. M. R. Louthan, Jr
Road 1A
Bldg. 773A, Rm. D-1153
Aiken, SC 29801

Distribution (continued)

MS-0960	N. DeMeza14100
MS-0958	A. Parker, 14184
MS-0958	C. Atwood, 14184
MS-0887	A. K. Hays, 1800
MS-0885	M. Cieslak, 1801
MS-1411	E. Fang, 1834
MS-1411	D. Dimos, 1843
MS-0367	Mark Smith, 1833
MS-0885	James Jellison, 1201
MS-9005	Rick Wayne, 2200
MS-9005	E. Cull Jr., 2260
MS-0319	Carl Vanecek, 2613
MS-0328	Marty Stevenson, 2612
MS-0319	Ken Eras, 2613
MS-0453	B. Damkroger. 2230
MS-9007	Doug Henson, 8400
MS-9108	M. Hardwick, 8414
MS-9403	Rick Stulen, 8700
MS-9401	Jill Hruby, 8702
MS-9402	W. Even, 8722
MS-9402	Ken Wilson, 8724
MS-9402	Annette Newman, 8724
MS-9042	W. Kawahara, 8725
MS-9404	Neville. Moody, 8725
MS-9161	E. P. Chin. 8726
MS-9042	Jim Handrock, 8727
MS-1411	Tom Headley, 1822
MS-0886	Don Susan, 1822
MS-1130	Joe Puskar, 1833
MS-9403	Nancy Yang, 8732
MS-9404	Steve Goods, 8725

5	MS-0367	Charlie Robino, 1833
5	MS-9402	John Brooks, 8724
5	MS-0958	M. Griffith, 14184
3	MS-9018	Central Technical Files, 8940-2
1	MS-0899	Technical Library, 4916
1	MS-9021	Classification Office, 8511/ Techncial Library, MS 0899, 4916
1	MS-9021	Classification Office 8511 for DOE/OSTI
1	MS-0188	D. Chavez, LDRD Office, 4001